12-2009

Integral Formulation of the Compressible Flowfield in Solid Rocket Motors

Michel Henry Akiki
University of Tennessee - Knoxville

To the Graduate Council:

I am submitting herewith a thesis written by Michel Henry Akiki entitled "Integral Formulation of the Compressible Flowfield in Solid Rocket Motors." I have examined the final electronic copy of this thesis for form and content and recommend that it be accepted in partial fulfillment of the requirements for the degree of Master of Science, with a major in Aerospace Engineering.

Joseph Majdalani, Major Professor

We have read this thesis and recommend its acceptance:

Basil Antar, Trevor Moeller

Accepted for the Council:
Carolyn R. Hodges

Vice Provost and Dean of the Graduate School

(Original signatures are on file with official student records.)

To the Graduate Council:

I am submitting herewith a thesis written by Michel Henry Akiki entitled “Integral Formulation of the Compressible Flowfield in Solid Rocket Motors.” I have examined the final electronic copy of this thesis for form and content and recommend that it be accepted in partial fulfillment of the requirements for the degree of Master of Science, with a major in Aerospace Engineering.

Joseph Majdalani, Major Professor

We have read this thesis
and recommend its acceptance:

Basil Antar

Trevor Moeller

Accepted for the Council:

Carolyn R. Hodges
Vice Provost and Dean of the Graduate School

(Original signatures are on file with official student records.)

Integral Formulation of the Compressible Flowfield in Solid Rocket Motors

A Thesis Presented for

the Master of Science

Degree

The University of Tennessee, Knoxville

Michel Henry Akiki

December 2009

Acknowledgments

I would like to thank my precious parents who escorted my steps to where I am today. I am grateful for my family, for their love and support. I would like to express my gratitude for my advisor, Dr. Majdalani, for his guidance throughout my graduate academic life. My committee, Dr. Moeller and Dr. Antar, also have my appreciation for their comments that helped improve this work. I would also like to acknowledge the National Science Foundation and The University of Tennessee Space Institute for their sponsorship.

Abstract

In this thesis, a semi-analytical formulation is provided for the rotational, steady, inviscid, compressible motion in a solid rocket motor that is modeled as a slender porous chamber. The analysis overcomes some of the deficiencies encountered in previous work on the subject. The method that we employ consists of reducing the problem's mass, momentum, energy, ideal gas, and isentropic relations into a single integral equation that can be solved numerically. Furthermore, Saint-Robert's power law is used to link the pressure to the sidewall mass injection rate. At the outset, results are presented for the axisymmetric and planar porous chambers and compared to two closed-form analytical solutions developed under one-dimensional and two-dimensional, isentropic flow conditions, in addition to experimental data. The comparison is carried out assuming either uniformly distributed mass flux or constant injection speed along the porous wall. Our amended formulation is shown to agree with the one-dimensional solution obtained for the case of uniform wall mass flux and with the asymptotic approximation for the constant wall injection speed.

Table of Contents

List of Figures

Nomenclature

c_p	=	constant pressure specific heat
L_0	=	length of chamber
L_s	=	sonic length (critical distance)
M	=	Mach number
m	=	injection mass flux
P	=	nondimensional pressure
p	=	dimensional pressure
r	=	coordinate normal to the propellant surface
T	=	temperature
U_w	=	wall injection velocity
u	=	axial velocity
v	=	radial velocity
X	=	nondimensional axial coordinate
x	=	dimensional axial coordinate

y = coordinate normal to the propellant surface

Greek

ψ = stream function

χ = axial coordinate referenced to the sonic length, x / L_s

γ = ratio of specific heats

ρ = density

ξ = distance from the headwall to the tip of the streamline at the sidewall

Chapter 1

Introduction

Rocket propulsion has been the sole means of transportation for spaceflights due to their independence of the surrounding environment. Like other forms of propulsion, rockets expend energy to produce thrust via an exchange of momentum with some reaction mass. While airplanes use the air to provide the reaction mass, rockets are self-supportive.

In chemical rockets, the propellant is ignited to transfer energy and accelerate the gaseous products to produce the desired thrust. Three families of engines are available; solid, liquid, and hybrid rocket engines. In solid rocket motors (SRMs), the fuel and oxidizer are premixed to form the propellant. Although they cannot be throttled and are relatively inefficient fuel burners, SRMs are simple to build and operate. Liquid rockets utilize liquid fuel and oxidizer stored in tanks and then pumped into a chamber for mixing and ignition. These engines provide high thrust capabilities and can be throttled. On the downside, liquid rockets are expensive and difficult to build. As for hybrid

rockets, a liquid oxidizer is injected into a chamber with a solid fuel grain covering the walls. Hybrids seem to combine the simplicity feature of solids and thrust capabilities of liquids. In addition to their throttling capabilities, they are less hazardous to work with. Among their drawbacks, hybrids exhibit lower combustion efficiencies due to incomplete mixing in the combustion zone.

The work in this thesis investigates the steady, inviscid, compressible mean flow field in solid rocket motors. These are often idealized as porous channels and ducts in which the effects of compressibility can be either retained or dismissed, depending on the gas injection speed and chamber length.

1.1 Incompressible Studies

Among the first investigations which modeled the fluid motion in porous chambers is a study furnished by Berman [1]. Using a stream function approach, Berman solves for the steady, viscous, incompressible flow field. In his work, the normal velocity is considered independent of the axial position such that, using a stream function approach, Berman derives a similarity reduced equation. Assuming a small injection velocity at the wall, his expansion uses a Reynolds number as a perturbation parameter.

In modeling internal flows fields, Taylor investigates the flow in wedges, cones and chambers with permeable walls [2]. Using an integral form of the continuity equation, he derives an incompressible, inviscid, steady state solution to the problem. Taylor presents the axial velocity profiles as cosine functions, for both the planar and cylindrical geometries.

In a study more applicable to rocketry, Culick [3] uses a differential stream function approach to solve for the incompressible flow field. In his attempt to understand the influence of mass injection on the mean and unsteady components of motion, he derives a simple yet highly useful model. In fact, Culick's profile may be considered one of the most fundamental in solid rocket motor theory.

While the incompressible motion is relatively well understood, [3, 4] recent advances have enabled us to account for the presence of arbitrary headwall injection [5, 6], wall regression [7, 8], grain taper [9, 10], and variable cross-section [11]. Furthermore, flow approximations exhibiting smoother or steeper profiles than the cold flow equilibrium state have been studied in connection with their energy content [12, 13].

1.2 Compressible Studies

As for compressible flow effects, these have been first investigated by Dunlap, Willoughby and Hermsen [14], and Traineau, Hervat and Kuentzmann [15] in the context of two-dimensional porous tubes and channels with sidewall injection. Using either Nitrogen or air as the working substance, these investigators have reported rich characteristics of the spatially developing motion including appreciable steepening beyond the Taylor-Culick baseline [3, 4]. In the downstream sections of the domain, compressibility intensified to the extent of producing noticeably flattened mean flow profiles. These observations were further supported by numerical simulations attributed to Beddini [16], Baum, Levine and Lovine [17], Liou and Lien [18], and Apte and Yang [19, 20]. They were also studied by Gany and Aharon [21] and King [22] in the context of nozzleless rocket motors. While the former group explored the merits of a one-

dimensional theoretical model, the latter employed a pseudo two-dimensional numerical approach. Given the relevance of an accurate mean flow description to the study of hydrodynamic instability in simulated rocket motors, the problem was revisited by Venugopal, Najjar and Moser [23] and, in complementary work, by Wasistho, Balachandar, and Moser [24]. As a windfall, the compressible solutions engendered in these studies proved to be valuable resources for verifying numerical results obtained from full-scale Navier-Stokes solvers [25, 26]. This was partly caused by the obstacles placed against the acquisition of specific experimental data and, partly, because of the intrusion-resistant environment in rocket chambers.

1.3 Analytical Models

Among the analytical techniques that have been applied to this problem, the first may be the Prandtl-Glauert expansion [27]. In fact, a variant of this technique was used by Traineau, Hervat and Kuentzmann [15] who introduced, in a precursor to the present study, an inviscid, rotational, and compressible integral equation that can be solved in a planar, two dimensional setting. In addition to their elegant analytical and numerical work, they produced a collection of experimental data based on cold flow measurements that utilized air as the sidewall injectant. In their analytical effort, these investigators dismissed the transverse static pressure gradient and reduced the velocity in the mass balance to its axial component. In this manner, the remaining momentum, mass, energy, ideal gas, and isentropic state relations are reduced to a single integral expression that can be numerically solved for the pressure distribution. Their Abel integral equation could be

shown to be soluble analytically in the case for which $2(2-\gamma)/(\gamma-1)$ took on an integer value.

In a similar work, Balakrishnan, Liñan and Williams [28] sought to reconstruct an inviscid, rotational, and compressible integral formulation for the porous channel problem. They utilized judicious scaling arguments to justify the dismissal of the radial momentum equation. In their study, the pressure and wall mass flux were related through the Saint-Robert power law.

The second analytical approach used in this context consists of a variant of the Rayleigh-Janzen expansion. This asymptotic technique is based on small parameter perturbations in the square of the wall injection Mach number. The approach requires the characteristic wall Mach number to be small, which makes it suitable for rocket motor applications. The Rayleigh-Janzen expansion was first applied by Majdalani [29] in the treatment of the axisymmetric porous cylinder and by Maicke and Majdalani [30] in the planar flow analog. The axisymmetric analysis led to two closed-form solutions, one exact, satisfying all first principles, and one approximate, essentially equivalent alternative. The planar effort gave rise to a single compact expression satisfying all physical requirements. In consequence, both streamwise and wall-normal velocity profiles could be readily calculated in addition to the critical length needed to achieve sonic conditions. Moreover, the effort led to the identification of the sonic distance as the appropriate lengthscale which, when inserted into the solution, would promote a self-similar, parameter-independent behavior for all wall Mach numbers. It also disclosed a simple criterion that could help to determine the relative effects of compressibility and

the centerline amplification during flow development. By circumventing the need to compute the mean flow over the fluid domain, the resulting expressions opened up new avenues for carrying out parametric trade analyses.

With the advent of a closed-form analytical solution for the internal burning porous cylinder in two dimensions, it is the purpose of this study to reconstruct the integral formulation developed initially by Traineau, Hervat and Kuentzmann [15] and later extended by Balakrishnan, Liñan and Williams [31]. Our objective is to obtain a clear and verifiable pseudo-two-dimensional approximation that could be compared to the one- and two-dimensional closed-form representations. To this end, both axisymmetric and planar configurations will be considered in the context of compressible inviscid flow through a rigid-cylindrical or rectangular chamber with porous sidewalls.

In this thesis, an integral formulation is used to solve for the compressible flow field in a solid rocket motor. In Chapter 2, the governing equations for the flow field are derived, in addition to the description of the boundary conditions. The procedure employed to reach the solution is described in Chapter 3, for both topographical configurations. Chapter 4 presents the results with comparisons to previous analytical and experimental verifications. Finally, results are summarized in Chapter 5 which includes a discussion of possible extensions to this work.

Chapter 2

Problem Definition

2.1 Geometry

A solid rocket motor is often idealized as a slender, elongated chamber with sidewall injection [28, 31]. Figure 2.1 portrays the chamber in both 2D and axisymmetric geometries, showing the origin of the coordinate system at the vertical center of the headwall. The chamber has a length L_0 and half height a that define its slenderness. In this work, we assume that $a / L_0 \ll 1$. As shown by Zhou and Majdalani [7], the effects of propellant regression are sufficiently small in the operational range of most motors, that they can be ignored. The burning propellant is modeled as a non-regressing porous wall injecting normally into the flow.

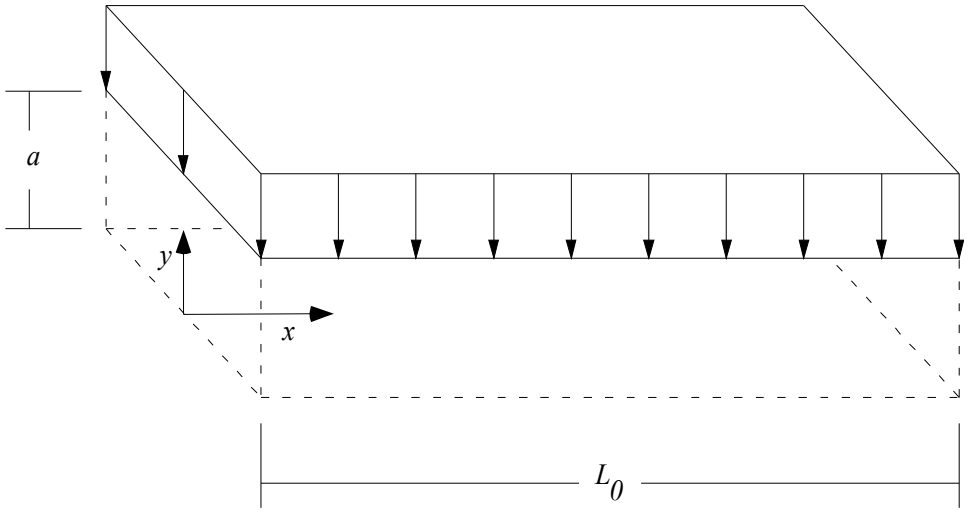

a)

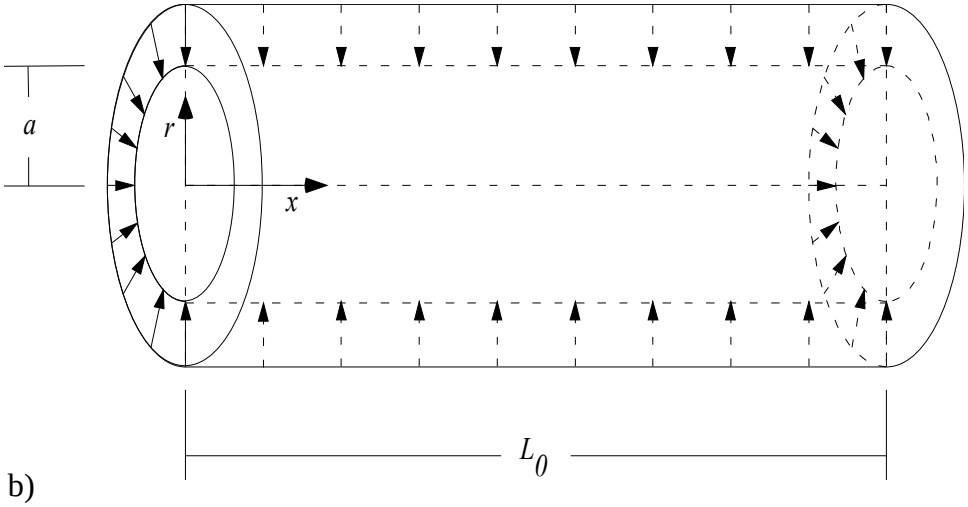

b)

Figure 2.1. Slender chamber with sidewall injection for a) planar and b) axisymmetic geometries.

2.2 Governing Equations

The purpose of this work is to solve for the internal, compressible flow field of a solid rocket motor chamber in both planar and cylindrical geometries. The assumptions used to idealize and simplify the problem include steady-state conditions, inviscid flow of an ideal gas and isentropic motion. At the centerline, the viscous boundary layer that may arise is not considered.

2.2.1 Conservation of Mass

For steady motions, the continuity equation reduces to

$$\nabla \cdot \left(\rho \boldsymbol{V} \right) = \vec{0} \tag{2.1}$$

The velocity vector $\boldsymbol{V}$ is composed of the axial and normal components denoted by u and v respectively. The gradient of the velocity results in

$$\frac{\partial \left(\rho u r \right)}{\partial x} + \frac{\partial \left(\rho v r \right)}{\partial r} = 0 \text{ (cylindrical coordinates)} \tag{2.2}$$

$$\frac{\partial \left(\rho u \right)}{\partial x} + \frac{\partial \left(\rho v \right)}{\partial y} = 0 \text{ (cartesian coordinates)} \tag{2.3}$$

2.2.2 Conservation of Momentum

The conservation of momentum equations may be reduced according to the assumptions listed above. At the outset, we get

$$\rho u \frac{\partial u}{\partial x} + \rho v \frac{\partial u}{\partial r} = -\frac{\partial p}{\partial x} \text{ (axial momentum)} \tag{2.4}$$

$$\rho u \frac{\partial v}{\partial x} + \rho v \frac{\partial v}{\partial r} = -\frac{\partial p}{\partial r} \text{ (radial momentum)} \tag{2.5}$$

By means of scaling analysis, we can simplify the equations significantly. The physical examination of the problem reveals that the radial velocity has the same order of magnitude as the injection velocity. The domain of the problem states that x scales like L_0 and r like a, and from the continuity equation, one can work out the order of magnitude of the axial velocity.

$$\frac{O\left(u\right)}{O\left(L_0\right)} + \frac{O\left(U_w\right)}{O\left(a\right)} = 0 \tag{2.6}$$

Therefore, u is of order $U_w L_0 / a$, and since $a / L_0 \ll 1$, then $u \gg v$. From Eqs. (2.4) and (2.5), the two pressure gradients can be deduced by recognizing a balance between pressure forces and inertia, namely

$$\frac{\partial p}{\partial x} \sim \frac{U_w^2}{a}\frac{L_0}{a} \qquad \frac{\partial p}{\partial r} \sim \frac{U_w^2}{a} \tag{2.7}$$

At any point in the fluid, the pressure, in general, is a function of both x and y and consequently, the total derivative is represented as

$$\mathrm{d}p = \frac{\partial p}{\partial x}\mathrm{d}x + \frac{\partial p}{\partial r}\mathrm{d}r \tag{2.8}$$

The ratio of the second term divided by the first term scales as

$$\frac{\frac{\partial p}{\partial r}\mathrm{d}r}{\frac{\partial p}{\partial x}\mathrm{d}x} \sim \left(\frac{a}{L_0}\right)^2 \ll 1 \tag{2.9}$$

In conclusion, the total derivative can be written as

$$\frac{\mathrm{d}p}{\mathrm{d}x} = \frac{\partial p}{\partial x} \tag{2.10}$$

This means that the pressure in the chamber, due its slenderness, varies mainly in the axial direction. This scaling analysis results in a significant simplification of the radial momentum equation by virtue of

$$\frac{\partial p}{\partial r} = 0 \text{ (cylindrical coordinates)} \tag{2.11}$$

$$\frac{\partial p}{\partial y} = 0 \text{ (cartesian coordinates)} \tag{2.12}$$

The axial momentum equation becomes

$$\rho u \frac{\partial u}{\partial x} + \rho v \frac{\partial u}{\partial r} = -\frac{\mathrm{d}p}{\mathrm{d}x} \text{ (cylindrical coordinates)} \tag{2.13}$$

$$\rho u \frac{\partial u}{\partial x} + \rho v \frac{\partial u}{\partial y} = -\frac{\mathrm{d}p}{\mathrm{d}x} \text{ (cartesian coordinates)} \tag{2.14}$$

2.2.3 Conservation of Energy

For a steady, adiabatic flow, without volume forces, the energy equation reduces to

$$\rho \boldsymbol{V} \cdot \nabla \left(h + \frac{1}{2} V^2 \right) = 0 \tag{2.15}$$

Assuming for this problem that the gas is calorically perfect, the specific heat at constant pressure becomes invariable over the domain defined. In this case, the enthalpy can be written in terms of the temperature. In reference to the solution of the order-of-magnitude analysis, v^2 could be safely neglected when added to the much larger u^2 and consequently, V^2 could be approximated and replaced by u^2. As a result, Eq. (2.15) reduces to

$$\rho u \frac{\partial}{\partial x}\left(c_p T + \frac{u^2}{2} \right) + \rho v \frac{\partial}{\partial r}\left(c_p T + \frac{u^2}{2} \right) = 0 \text{ (cylindrical coordinates)} \qquad (2.16)$$

$$\rho u \frac{\partial}{\partial x}\left(c_p T + \frac{u^2}{2} \right) + \rho v \frac{\partial}{\partial y}\left(c_p T + \frac{u^2}{2} \right) = 0 \text{ (cartesian coordinates)} \qquad (2.17)$$

The right hand side of Eqs. (2.16) and (2.17) are by definition the material derivative of the term $\left(c_p T + \frac{1}{2} u^2 \right)$, which, for a fluid particle, gives

$$c_p T + \frac{u^2}{2} = \text{constant} \qquad (2.18)$$

However, in a steady flow, particle paths coincide with streamlines, which makes Eq. (2.18) valid for each streamline. The constant may be different for distinct streamlines albeit dependent on the originating point at the wall.

2.3 Boundary Conditions

The physical requirements of the problem are used to define a consistent set of boundary conditions. We begin at the sidewall which can be viewed as a porous plate injecting fluid into the chamber with a velocity normal to the injection plane. This condition requires the axial velocity along the porous plate to vanish. Concerning the injection velocity, it is allowed to vary with the longitudinal distance from the headwall and is later linked to the chamber pressure through Saint-Robert's law. The temperature of the wall is also taken as a function of the distance from the headwall. Since the geometry is symmetrical with respect to the centerline, our solution will consider half of the chamber, and set the axis as a boundary with conditions of symmetry. Accordingly, no cross-flow will be permitted along the centerline. At the inert headwall, injection is

suppressed and the pressure is set to p_0. In cylindrical coordinates, these boundary conditions translate into:

$$\begin{cases} u(x,a) = 0 & \text{(no slip at sidewall)} \\ u(0,r) = 0 & \text{(no headwall injection)} \\ v(x,a) = -U_w(x) & \text{(radial sidewall injection)} \\ v(x,0) = 0 & \text{(no cross-flow at the centerline)} \\ T(x,a) = T_w(x) & \text{(sidewall temperature)} \\ p(0) = p_0 & \text{(headwall pressure)} \end{cases} \tag{2.19}$$

In cartesian coordinates, the boundary conditions remain the same except for the r coordinate being replaced by y.

Now that the governing equations and boundary conditions have been fully defined, the problem is ready to be tackled.

Chapter 3

Solution Formulation

3.1 Axisymmetric Configuration

We consider the steady, inviscid flow of an ideal gas in a cylinder of length L_0 and radius a. A schematic diagram of the problem is presented in Figure 3.1. The origin of the coordinate system is located at the center of the headwall. Due to axisymmetry,

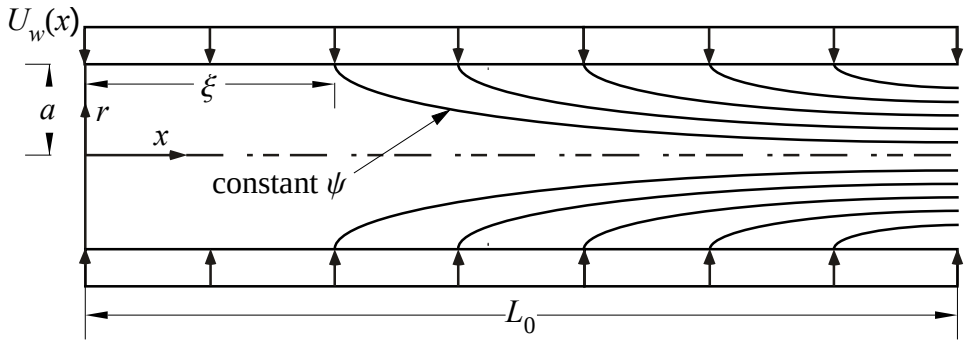

Figure 3.1. Schematic diagram of a slender porous cylinder.

only half of the chamber will be investigated. Note that ψ represents a streamline and ξ denotes the axial distance from the headwall to the point where a streamline is born at the sidewall, thus marking the tip of a streamline.

3.1.1 Formulation

In Section 2.2, the governing equations were derived for the problem at hand. With the assumption of a low chamber aspect ratio, $a / L_0 \ll 1$, the system's conservation laws may be conveniently reduced to the following set:

$$\frac{\partial(\rho u r)}{\partial x} + \frac{\partial(\rho v r)}{\partial r} = 0 \text{ (compressible continuity)} \tag{3.1}$$

$$\rho u \frac{\partial u}{\partial x} + \rho v \frac{\partial u}{\partial r} = -\frac{\partial p}{\partial x} \text{ (axial momentum)} \tag{3.2}$$

$$\frac{\partial p}{\partial r} = 0 \text{ (radial momentum)} \tag{3.3}$$

and

$$\rho u \frac{\partial}{\partial x}\left(c_p T + \frac{u^2}{2}\right) + \rho v \frac{\partial}{\partial r}\left(c_p T + \frac{u^2}{2}\right) = 0 \text{ (energy)} \tag{3.4}$$

Note that pressure variations have been discounted in the radial direction due to the chamber's low aspect ratio. Furthermore, the gas may be taken to be ideal and calorically perfect, thus resulting in a constant c_p. At the outset, one may write

$$p = \frac{\gamma - 1}{\gamma} c_p \rho T \text{ (ideal gas)} \tag{3.5}$$

At this point, Eq. (3.4) may be expanded and rearranged into

$$\rho u c_p \frac{\partial T}{\partial x} + \rho v c_p \frac{\partial T}{\partial r} + u\left(\rho u \frac{\partial u}{\partial x} + \rho v \frac{\partial u}{\partial r} \right) = 0 \tag{3.6}$$

Both Eqs. (3.2) and (3.5) may be substituted into Eq. (3.6) to produce

$$\rho u \left(\frac{\partial T}{\partial x} - \frac{\gamma - 1}{\gamma} \frac{T}{p} \frac{\partial p}{\partial x} \right) + \rho v \frac{\partial T}{\partial r} = 0 \tag{3.7}$$

Finally, inserting the isentropic state relation expression, $\phi = T / p^{\left[(\gamma-1)/\gamma\right]}$, into Eq. (3.7), one obtains

$$\rho u \frac{\partial \phi}{\partial x} + \rho v \frac{\partial \phi}{\partial y} = 0, \quad \rho \boldsymbol{u} \cdot \nabla \phi = 0, \quad \text{or} \quad \rho \frac{\mathrm{D}\phi}{\mathrm{D}t} = 0 \tag{3.8}$$

Since the material derivative vanishes in Eq. (3.8), it is clear that ϕ remains constant along a streamline.

3.1.2 Stream Function Transformation

For compressible axisymmetric motions, the stream function may be written as

$$\frac{\partial \psi}{\partial r} = \rho u r, \quad \frac{\partial \psi}{\partial x} = -\rho v r \tag{3.9}$$

Given that the total energy, $\left(c_p T + u^2 / 2 \right)$, remains invariant along a streamline, one can put

$$T\left(x, \psi\right) + u^2\left(x, \psi\right) / (2c_p) = T_w\left(\psi\right) \tag{3.10}$$

where $T_w\left(\psi\right)$ is the temperature at the wall. Likewise for ϕ, the isentropic pressure-temperature relation may be expressed as

$$T\left(x,\psi\right)/\left[p\left(x\right)\right]^{\left(\gamma-1\right)/\gamma}=T_w\left(\psi\right)/\left[p_w\left(\psi\right)\right]^{\left(\gamma-1\right)/\gamma} \tag{3.11}$$

Given that all streamlines are initiated through surface injection at $r=a$, Eq. (3.9) may be evaluated at the sidewall. This is performed while using the ideal gas expression for the density. Subsequent integration in the axial direction yields

$$\psi=\frac{a\gamma}{\left(\gamma-1\right)c_p}\int_0^{\xi}\left[U_w\left(x\right)p\left(x\right)/T_w\left(x\right)\right]\mathrm{d}x \tag{3.12}$$

As depicted in Figure 3.1, ξ denotes the distance from the headwall to the point where the streamline originates at the sidewall. Since a unique value of ψ associates itself with a given ξ, one may transform the independent variables from $\left(x,\psi\right)$ to $\left(x,\xi\right)$. In this new coordinate system, Eqs. (3.10) and (3.11) may be written as

$$T\left(x,\xi\right)+u^2\left(x,\xi\right)/\left(2c_p\right)=T_w\left(\xi\right) \tag{3.13}$$

$$T\left(x,\xi\right)/\left[p\left(x\right)\right]^{\left(\gamma-1\right)/\gamma}=T_w\left(\xi\right)/\left[p\left(\xi\right)\right]^{\left(\gamma-1\right)/\gamma} \tag{3.14}$$

Next, the expression for the stream function given by Eq. (3.12) may be substituted into Eq. (3.9) and integrated in the radial direction. This enables us to deduce the coordinate r corresponding to a given axial position x and streamline emanating from ξ:

$$r^2=2a\int_0^{\xi}\left[\frac{T\left(x,\xi'\right)}{p\left(x\right)u\left(x,\xi'\right)}\right]\left[\frac{U_w\left(\xi'\right)p\left(\xi'\right)}{T_w\left(\xi'\right)}\right]\mathrm{d}\xi' \tag{3.15}$$

One can also replace the variables u and T using Eqs. (3.13) and (3.14) to produce an expression solely in terms of the pressure. This operation yields

$$r^2 = 2a\int_0^{\xi}\left[\frac{p\left(\xi'\right)}{p\left(x\right)}\right]^{1/\gamma}\left[1-\left[\frac{p\left(x\right)}{p\left(\xi'\right)}\right]^{\left(\gamma-1\right)/\gamma}\right]^{-1/2}\frac{U_w\left(\xi'\right)}{\sqrt{2c_pT_w\left(\xi'\right)}}\,\mathrm{d}\xi' \tag{3.16}$$

At this point, we are ready to evaluate Eq. (3.16) knowing that $\xi = x$ at $r = a$; we get

$$a = 2\int_0^{x}\left[\frac{p\left(\xi\right)}{p\left(x\right)}\right]^{1/\gamma}\left[1-\left[\frac{p\left(x\right)}{p\left(\xi\right)}\right]^{\left(\gamma-1\right)/\gamma}\right]^{-1/2}\frac{U_w\left(\xi\right)}{\sqrt{2c_pT_w\left(\xi\right)}}\,\mathrm{d}\xi \tag{3.17}$$

3.1.3 Integral Formulation with No Pressure Dependence

The dimensionless variables $P(X)$, X and Ξ may be introduced to simplify the analysis. These are defined according to

$$P\left(X\right) = \frac{p\left(x\right)}{p_0} \tag{3.18}$$

$$X = \sqrt{\frac{\gamma}{\gamma-1}}\frac{1}{a}\int_0^{x}\frac{U_w\left(x'\right)}{\sqrt{2c_pT_w\left(x'\right)}}\,\mathrm{d}x' = \sqrt{\frac{\gamma}{2}}\frac{1}{a}\int_0^{x}M_w\left(x'\right)\mathrm{d}x' \tag{3.19}$$

$$\Xi = \sqrt{\frac{\gamma}{\gamma-1}}\frac{1}{a}\int_0^{\xi}\frac{U_w\left(x'\right)}{\sqrt{2c_pT_w\left(x'\right)}}\,\mathrm{d}x' = \sqrt{\frac{\gamma}{2}}\frac{1}{a}\int_0^{\xi}M_w\left(x'\right)\mathrm{d}x' \tag{3.20}$$

While the normalization of P is straightforward, that of X and Ξ is based on their upper integral bounds. Then, dimensionless expressions are inserted into Eqs. (3.16) and (3.17) to obtain

$$\left(\frac{r}{a}\right)^2 = 2\sqrt{\frac{\gamma-1}{\gamma}}\int_0^{\Xi}\left[\frac{P\left(\Xi'\right)}{P\left(X\right)}\right]^{1/\gamma}\left[1-\left(\frac{P\left(X\right)}{P\left(\Xi'\right)}\right)^{\left(\gamma-1\right)/\gamma}\right]^{-1/2}\mathrm{d}\Xi' \tag{3.21}$$

$$\sqrt{\frac{\gamma}{\gamma-1}} = 2\int_0^X \left[\frac{P(\Xi)}{P(X)}\right]^{1/\gamma} \left[1-\left(\frac{P(X)}{P(\Xi)}\right)^{(\gamma-1)/\gamma}\right]^{-1/2} d\Xi \tag{3.22}$$

Equations (3.21) and (3.22) differ from the result obtained by Balakrishnan, Liñan and Williams [28] who include an extra (Ξ / X) term as part of their integrand.

3.1.4 Integral Formulation with Pressure Dependence

In reality, the mass flux generated by the propellant at the wall is not uniform along the length of the chamber but rather depends on flow conditions. A good model that links $m_w(\xi)$ to $p(\xi)$ is Saint-Robert's law with constant K and n,

$$m_w = \rho_w U_w = K p^n \tag{3.23}$$

where m_w represents the mass flux at the wall. Then using the ideal gas law to eliminate the density, the injection velocity may be expressed as

$$U_w = \left(\frac{\gamma-1}{\gamma}\right) c_p \frac{T_w(\xi)}{p(\xi)} m_w(\xi) \tag{3.24}$$

Examining Eq. (3.23), we notice that for $n=0$, the injection mass flow rate becomes constant along the wall. Whereas for $n=1$, we notice from Eq. (3.24) that a uniform injection velocity becomes established along the length of the grain. After substituting the above into Eq. (3.21), the dimensionless forms of $P(X), X$ and Ξ may be written as

$$P(X) = \frac{p(x)}{p_0} \tag{3.25}$$

$$X = \sqrt{\frac{\gamma-1}{\gamma}}\frac{Kp_0^{n-1}}{2a}\int_0^x \sqrt{2c_p T_w\left(x'\right)}\mathrm{d}x' \tag{3.26}$$

$$\Xi = \sqrt{\frac{\gamma-1}{\gamma}}\frac{Kp_0^{n-1}}{2a}\int_0^\xi \sqrt{2c_p T_w\left(x'\right)}\mathrm{d}x' \tag{3.27}$$

At length, Eqs. (3.16) and (3.17) become

$$\left(\frac{r}{a}\right)^2 = 2\sqrt{\frac{\gamma-1}{\gamma}}\int_0^\Xi \left[P\left(\Xi'\right)\right]^{n-1}\left[\frac{P\left(\Xi'\right)}{P\left(X\right)}\right]^{1/\gamma}\left[1-\left(\frac{P\left(X\right)}{P\left(\Xi'\right)}\right)^{(\gamma-1)/\gamma}\right]^{-1/2}\mathrm{d}\Xi' \tag{3.28}$$

$$\sqrt{\frac{\gamma}{\gamma-1}} = 2\int_0^X \left[P\left(\Xi\right)\right]^{n-1}\left[\frac{P\left(\Xi\right)}{P\left(X\right)}\right]^{1/\gamma}\left[1-\left(\frac{P\left(X\right)}{P\left(\Xi\right)}\right)^{(\gamma-1)/\gamma}\right]^{-1/2}\mathrm{d}\Xi \tag{3.29}$$

The procedure for solving this problem consists of integrating Eq. (3.29) to the extent of determining the pressure as a function of x. Equation (3.28) can then be evaluated to deduce the radial coordinate in terms of x and ξ. With the pressure distribution at hand, the temperature can be obtained using the isentropic relation of Eq. (3.14). The velocity may then be extracted from the total temperature relation given by Eq. (3.13).

For the calculation of the Mach number, one can employ the compressible flow relation $M = u/\sqrt{\left(\gamma-1\right)c_p T}$. In fact, the substitution of Eq. (3.13) into the Mach number relation yields

$$M = \sqrt{\left(\frac{2}{\gamma-1}\right)\left[\frac{T_w\left(\xi\right)}{T\left(x,\xi\right)}-1\right]} = \sqrt{\left(\frac{2}{\gamma-1}\right)\left[\left(\frac{P\left(\Xi\right)}{P\left(X\right)}\right)^{(\gamma-1)/\gamma}-1\right]} \tag{3.30}$$

where the right-hand-side expression may be obtained using the isentropic identity given by Eq. (3.14).

3.1.5 Numerical Procedure

For the numerical integration of Eq. (3.29), an inverse procedure may be pursued. This is accomplished by switching to P as the independent variable and calculating X in increments of ΔP The scheme begins at the headwall boundary, where $X = 0$ at $P = 1$. Choking conditions occur when $\mathrm{d}P / \mathrm{d}X \to \infty$ Transforming the independent variable in Eq. (3.29) results in

$$2\sqrt{\frac{\gamma-1}{\gamma}}\int_P^1 \left(P'\right)^{n-1}\left(\frac{P'}{P}\right)^{1/\gamma}\left[1-\left(\frac{P}{P'}\right)^{(\gamma-1)/\gamma}\right]^{-1/2}\left[-\frac{\mathrm{d}X\left(P'\right)}{\mathrm{d}P'}\right]\mathrm{d}P' = \int_P^1 f\left(P'\right)\mathrm{d}P' = 1 \quad (3.31)$$

In order to overcome the singularities at the boundaries, we split the integral into three parts:

$$\int_P^1 f\left(P'\right)\mathrm{d}P' = \underbrace{\int_{P_i}^{P_{i-1}} f\left(P'\right)\mathrm{d}P'}_{1} + \underbrace{\int_{P_{i-1}}^{1-\Delta P} f\left(P'\right)\mathrm{d}P'}_{2} + \underbrace{\int_{1-\Delta P}^{1} f\left(P'\right)\mathrm{d}P'}_{3} = 1 \quad (3.32)$$

In the region near $P = P_i$, we approximate the first integrand and retrieve an expression that can be readily evaluated for an arbitrary pressure exponent n,

$$\int_{P_i}^{P_{i-1}} f\left(P'\right)\mathrm{d}P' \approx 2\int_{P_i}^{P_{i-1}} \left(P'\right)^{n-1}\left(\frac{P'-P_i}{P'}\right)^{-1/2}\left(-\frac{\mathrm{d}X}{\mathrm{d}P}\right)_i \mathrm{d}P' \quad (3.33)$$

For $n = 0$

$$\int_{P_i}^{P_{i-1}} f\left(P'\right)\mathrm{d}P' \approx 4\ln\left(\frac{\sqrt{P_i + \Delta P} + \sqrt{\Delta P}}{\sqrt{P_i}}\right)\frac{\left(X_i - X_{i-1}\right)}{\Delta P}$$

For $n = 1$ (3.34)

$$\int_{P_i}^{P_{i-1}} f\left(P'\right)\mathrm{d}P' \approx 2\left[P_i \ln\left(\frac{\sqrt{P_i + \Delta P} + \sqrt{\Delta P}}{\sqrt{P_i}}\right) + \sqrt{\Delta P}\sqrt{\Delta P + P_i}\right]\frac{\left(X_i - X_{i-1}\right)}{\Delta P}$$

The second integral may be computed, for example, using the trapezoidal rule. This involves finite step discretization,

$$\int_{P_{i-1}}^{1-\Delta P} f\left(P'\right)\mathrm{d}P' \approx \Delta P\left(\frac{f_1 + f_{i-1}}{2} + \sum_{k=2}^{i-2} f_k\right) \tag{3.35}$$

where

$$f_k = 2\sqrt{\frac{\gamma - 1}{\gamma}}\left[P_k\right]^{n-1}\left[\frac{P_k}{P_i}\right]^{1/\gamma}\left[1 - \left(\frac{P_i}{P_k}\right)^{(\gamma-1)/\gamma}\right]^{-1/2}\left(-\frac{\mathrm{d}X}{\mathrm{d}P}\right)_k \tag{3.36}$$

In the third integral, where X is small, $P\left(X\right)$ may be expanded using a polynomial of the form

$$P\left(x\right) = 1 - \alpha X^2 + \ldots \tag{3.37}$$

By inserting Eq. (3.37) into the integral and assuming $\alpha\,\Xi^2 \ll 1$, we are left with

$$\int_{1-\Delta P}^{1} f\left(P'\right)\mathrm{d}P' \approx 2\sqrt{\frac{\gamma - 1}{\gamma}}\left(P_i\right)^{-1/\gamma}\left[1 - \left(P_i\right)^{(\gamma-1)/\gamma}\right]^{-1/2}\sqrt{\frac{\Delta P}{\alpha}} \tag{3.38}$$

To evaluate Eq. (3.38), α must be known beforehand. This is achieved by substituting Eq. (3.37) into Eq. (3.29) and returning

$$\frac{2}{\sqrt{\alpha}}\int_0^X \frac{1}{\sqrt{X^2-\Xi^2}}\,\mathrm{d}\Xi = 1 \tag{3.39}$$

This enables us to deduce that $\alpha = \pi^2$.

Equation (3.31) is now linear in X_i. Starting with $X = 0$ at $P = 1$, one may solve for X_i at every step until choking conditions are reached. Choking occurs at a point where P approaches its limiting value P_c at an infinitely steep slope and where the average Mach number reaches unity. With the pressure distribution fully determined, it may be inserted into Eq. (3.28) and integrated numerically. This returns r which is needed for the complete description of the streamlines. Equations (3.13) and (3.14) may then be utilized to extract the temperature and velocity. This process is illustrated in the flowchart diagram posted as Figure 3.2. Since the procedure requires solving for the axial and radial coordinates, the meshing takes place automatically, where every point is defined in a streamline coordinate system, $\left(x,\xi\right)$, as illustrated in Figure 3.3.

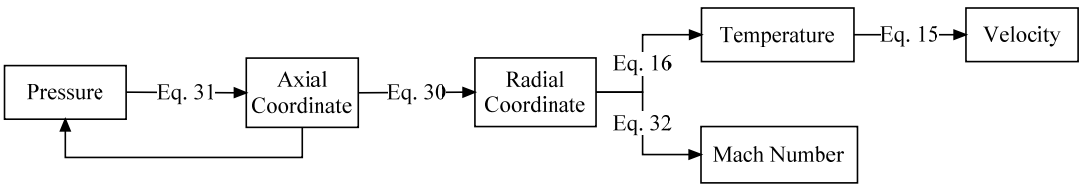

Figure 3.2. Flowchart depicting the main steps of the numerical procedure needed to extract the velocity from the integral formulation of the pressure.

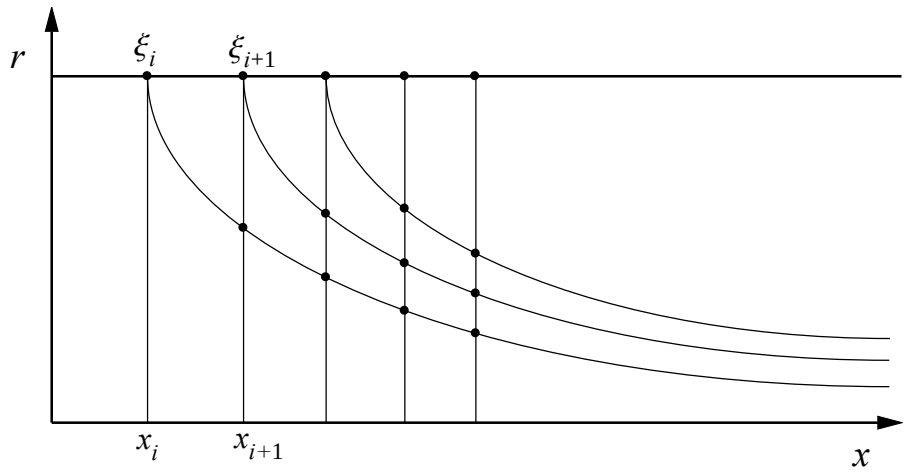

Figure 3.3. Illustration of the mesh generated.

3.2 Planar Configuration

Section 3.1 presents a quasi-two-dimensional integral approach to solve for the compressible mean flow in a cylindrical rocket motor. A similar analysis may be followed in constructing the solution in a rectangular chamber. A schematic diagram of the geometry is illustrated in Figure 3.4

3.2.1 Formulation

The domain under investigation extends horizontally from $x = 0$ to $x = L_0$, and vertically from the center axis to the wall, where the top and bottom plates may be viewed as symmetrical porous sidewalls across which flow is injected at a velocity $U_w\left(x\right)$. A schematic diagram of the planar problem is given in Figure 3.4. We start with the governing equations derived in Section 2.2 for the corresponding case.

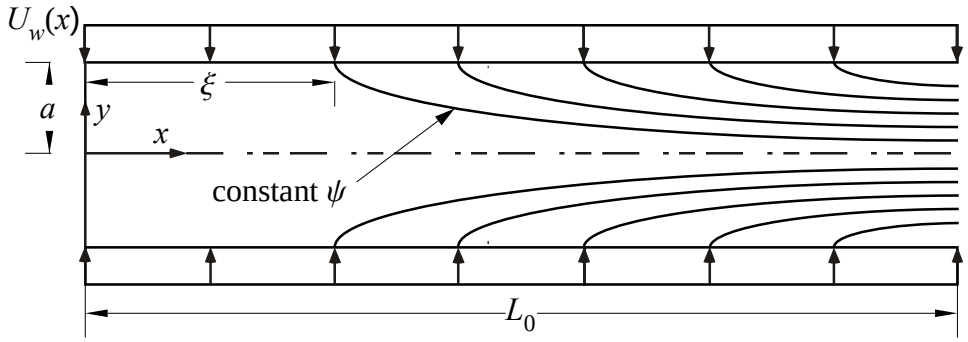

Figure 3.4. Schematic diagram of a slender porous chamber.

$$\frac{\partial(\rho u)}{\partial x}+\frac{\partial(\rho v)}{\partial y}=0 \text{ (compressible continuity)} \tag{3.40}$$

$$\rho u\frac{\partial u}{\partial x}+\rho v\frac{\partial u}{\partial y}=-\frac{\partial p}{\partial x} \text{ (x-momentum)} \tag{3.41}$$

$$\frac{\partial p}{\partial y}=0 \text{ (y-momentum)} \tag{3.42}$$

and

$$\rho u\frac{\partial}{\partial x}\left(c_pT+\frac{u^2}{2}\right)+\rho v\frac{\partial}{\partial y}\left(c_pT+\frac{u^2}{2}\right)=0 \text{ (energy)} \tag{3.43}$$

The gas is assumed to be ideal with a constant c_p such that

$$p=\frac{\gamma-1}{\gamma}c_p\rho T \text{ (ideal gas)} \tag{3.44}$$

For energy conservation, Eq. (3.43), may be rearranged into

$$\rho uc_p\frac{\partial T}{\partial x}+\rho vc_p\frac{\partial T}{\partial y}+u\left(\rho u\frac{\partial u}{\partial x}+\rho v\frac{\partial u}{\partial y}\right)=0 \tag{3.45}$$

The term that appears between parentheses is essentially the left-hand-side of the momentum equation. One can substitute Eqs. (3.41) and (3.44) into Eq. (3.45) to produce

$$\rho u\left(\frac{\partial T}{\partial x}-\frac{\gamma-1}{\gamma}\frac{T}{p}\frac{\partial p}{\partial x}\right)+\rho v\frac{\partial T}{\partial y}=0 \tag{3.46}$$

Then, inserting $\phi = T \,/\, p^{\left[(\gamma-1)/\gamma\right]}$ into Eq. (3.46), one obtains

$$\rho u\frac{\partial \phi}{\partial x}+\rho v\frac{\partial \phi}{\partial y}=0, \quad \rho \boldsymbol{u}\cdot\nabla\phi=0, \quad \text{or} \quad \rho\frac{\mathrm{D}\phi}{\mathrm{D}t}=0 \tag{3.47}$$

Equation (3.47) reminds us that ϕ remains constant along a streamline.

3.2.2 Stream Function Transformation

For planar flows, the stream function may be written as

$$\frac{\partial \psi}{\partial y}=\rho u, \quad \frac{\partial \psi}{\partial x}=-\rho v \tag{3.48}$$

With a constant $\left(c_p T+u^2\,/\,2\right)$ along a streamline, one can say

$$T\left(x,\psi\right)+u^2\left(x,\psi\right)/\left(2c_p\right)=T_w\left(\psi\right) \tag{3.49}$$

Similarly for ϕ, the isentropic pressure-temperature relation, at any point on of the streamline, is equal to its value at the wall and may be expressed as

$$T\left(x,\psi\right)/\left[p\left(x\right)\right]^{(\gamma-1)/\gamma}=T_w\left(\psi\right)/\left[p_w\left(\psi\right)\right]^{(\gamma-1)/\gamma} \tag{3.50}$$

Using the ideal gas expression for the density, subsequent integration in the x-direction yields

$$\psi = \frac{a\,\gamma}{\left(\gamma-1\right)c_p}\int_0^{\xi}\left[U_w\left(x\right)p\left(x\right)/T_w\left(x\right)\right]\mathrm{d}x \tag{3.51}$$

We now transform the independent variables from $\left(x,\psi\right)$ to $\left(x,\xi\right)$ and rewrite Eqs. (3.49) and (3.50) as

$$T\left(x,\xi\right)+u^2\left(x,\xi\right)/\left(2c_p\right)=T_w\left(\xi\right) \tag{3.52}$$

$$T\left(x,\xi\right)/\left[p\left(x\right)\right]^{\left(\gamma-1\right)/\gamma}=T_w\left(\xi\right)/\left[p\left(\xi\right)\right]^{\left(\gamma-1\right)/\gamma} \tag{3.53}$$

Next, the expression for the stream function given by Eq. (3.51) may be substituted into Eq. (3.48) and integrated in the normal direction. This enables us to extract the coordinate y associated with a given position x and the streamline emanating from an arbitrary position ξ at the sidewall:

$$y=\int_0^{\xi}\left[\frac{T\left(x,\xi'\right)}{p\left(x\right)u\left(x,\xi'\right)}\right]\left[\frac{U_w\left(\xi'\right)p\left(\xi'\right)}{T_w\left(\xi'\right)}\right]\mathrm{d}\xi' \tag{3.54}$$

To express y in terms of the pressure only, one can use Eqs. (3.52) and (3.53) to substitute for the velocity and temperature. This operation yields

$$y=\int_0^{\xi}\left[\frac{p\left(\xi'\right)}{p\left(x\right)}\right]^{1/\gamma}\left[1-\left[\frac{p\left(x\right)}{p\left(\xi'\right)}\right]^{\left(\gamma-1\right)/\gamma}\right]^{-1/2}\frac{U_w\left(\xi'\right)}{\sqrt{2c_pT_w\left(\xi'\right)}}\mathrm{d}\xi' \tag{3.55}$$

Recalling that $y=a$ at $\xi=x$, Eq. (3.55) may be recast in the form:

$$a=\int_0^{x}\left[\frac{p\left(\xi\right)}{p\left(x\right)}\right]^{1/\gamma}\left[1-\left[\frac{p\left(x\right)}{p\left(\xi\right)}\right]^{\left(\gamma-1\right)/\gamma}\right]^{-1/2}\frac{U_w\left(\xi\right)}{\sqrt{2c_pT_w\left(\xi\right)}}\mathrm{d}\xi \tag{3.56}$$

3.2.3 Integral Formulation with No Pressure Dependence

We now introduce the dimensionless variables $P(X)$, X and Ξ to simplify the analysis. These are defined as

$$P\left(X\right) = \frac{p\left(x\right)}{p_0} \tag{3.57}$$

$$X = \sqrt{\frac{\gamma}{\gamma-1}}\frac{1}{a}\int_0^x \frac{U_w\left(x'\right)}{\sqrt{2c_pT_w\left(x'\right)}}\mathrm{d}x' = \sqrt{\frac{\gamma}{2}}\frac{1}{a}\int_0^x M_w\left(x'\right)\mathrm{d}x' \tag{3.58}$$

$$\Xi = \sqrt{\frac{\gamma}{\gamma-1}}\frac{1}{a}\int_0^\xi \frac{U_w\left(x'\right)}{\sqrt{2c_pT_w\left(x'\right)}}\mathrm{d}x' = \sqrt{\frac{\gamma}{2}}\frac{1}{a}\int_0^\xi M_w\left(x'\right)\mathrm{d}x' \tag{3.59}$$

These dimensionless expressions may be inserted into Eqs. (3.55) and (3.56) to obtain

$$\frac{y}{a} = \sqrt{\frac{\gamma-1}{\gamma}}\int_0^\Xi \left[\frac{P\left(\Xi'\right)}{P\left(X\right)}\right]^{1/\gamma}\left[1-\left(\frac{P\left(X\right)}{P\left(\Xi'\right)}\right)^{(\gamma-1)/\gamma}\right]^{-1/2}\mathrm{d}\Xi' \tag{3.60}$$

$$\sqrt{\frac{\gamma}{\gamma-1}} = \int_0^X \left[\frac{P\left(\Xi\right)}{P\left(X\right)}\right]^{1/\gamma}\left[1-\left(\frac{P\left(X\right)}{P\left(\Xi\right)}\right)^{(\gamma-1)/\gamma}\right]^{-1/2}\mathrm{d}\Xi \tag{3.61}$$

3.2.4 Integral Formulation with Pressure Dependence

One can link $m_w\left(\xi\right)$ to $p\left(\xi\right)$ by assuming a dependence on the burning-rate that follows Saint-Robert's law with constant K and n,

$$m_w = \rho_w U_w = Kp^n \tag{3.62}$$

Then using the ideal gas law to eliminate the density, the injection velocity may be expressed as

$$U_w = \left(\frac{\gamma-1}{\gamma}\right) c_p \frac{T_w\left(\xi\right)}{p\left(\xi\right)} m_w\left(\xi\right) \tag{3.63}$$

After substituting the above into Eq. (3.56), the dimensionless forms of $P(X)$, X and Ξ may be retrieved. These are

$$P\left(X\right) = \frac{p\left(x\right)}{p_0} \tag{3.64}$$

$$X = \sqrt{\frac{\gamma-1}{\gamma}} \frac{K p_0^{n-1}}{2a} \int_0^x \sqrt{2c_p T_w\left(x'\right)}\mathrm{d}x' \tag{3.65}$$

$$\Xi = \sqrt{\frac{\gamma-1}{\gamma}} \frac{K p_0^{n-1}}{2a} \int_0^\xi \sqrt{2c_p T_w\left(x'\right)}\mathrm{d}x' \tag{3.66}$$

At length, Eqs. (3.55) and (3.56) become

$$\frac{y}{a} = \sqrt{\frac{\gamma-1}{\gamma}} \int_0^\Xi \left[P\left(\Xi'\right)\right]^{n-1} \left[\frac{P\left(\Xi'\right)}{P\left(X\right)}\right]^{1/\gamma} \left[1-\left(\frac{P\left(X\right)}{P\left(\Xi'\right)}\right)^{(\gamma-1)/\gamma}\right]^{-1/2} \mathrm{d}\Xi' \tag{3.67}$$

and

$$\sqrt{\frac{\gamma}{\gamma-1}} = \int_0^X \left[P\left(\Xi\right)\right]^{n-1} \left[\frac{P\left(\Xi\right)}{P\left(X\right)}\right]^{1/\gamma} \left[1-\left(\frac{P\left(X\right)}{P\left(\Xi\right)}\right)^{(\gamma-1)/\gamma}\right]^{-1/2} \mathrm{d}\Xi \tag{3.68}$$

Following the same procedure described in Section 3.1.4, we are now able to solve for the pressure, temperature and velocity profiles.

To calculate the Mach number, one can employ the compressible flow relation $M = u / \sqrt{\left(\gamma - 1\right) c_p T}$. In fact, the substitution of Eq. (3.52) into the Mach number relation gives

$$M = \sqrt{\left(\frac{2}{\gamma - 1}\right)\left[\frac{T_w\left(\xi\right)}{T\left(x,\xi\right)} - 1\right]} = \sqrt{\left(\frac{2}{\gamma - 1}\right)\left[\left(\frac{P\left(\Xi\right)}{P\left(X\right)}\right)^{\left(\gamma-1\right)/\gamma} - 1\right]} \tag{3.69}$$

where the right-hand-side expression may be obtained using the isentropic identity given by Eq. (3.53).

3.2.5 Numerical Procedure

The numerical procedure follows the same guidelines described in Section 3.1.5. Transforming the independent variable in Eq. (3.68) from X to P results in

$$\sqrt{\frac{\gamma - 1}{\gamma}} \int_P^1 \left(P'\right)^{n-1} \left(\frac{P'}{P}\right)^{1/\gamma} \left[1 - \left(\frac{P}{P'}\right)^{\left(\gamma-1\right)/\gamma}\right]^{-1/2} \left[-\frac{\mathrm{d}X\left(P'\right)}{\mathrm{d}P'}\right] \mathrm{d}P' = \int_P^1 f\left(P'\right) \mathrm{d}P' = 1 \tag{3.70}$$

The integral is split into three parts:

$$\int_P^1 f\left(P'\right) \mathrm{d}P' = \underbrace{\int_{P_i}^{P_{i-1}} f\left(P'\right) \mathrm{d}P'}_{1} + \underbrace{\int_{P_{i-1}}^{1-\Delta P} f\left(P'\right) \mathrm{d}P'}_{2} + \underbrace{\int_{1-\Delta P}^{1} f\left(P'\right) \mathrm{d}P'}_{3} = 1 \tag{3.71}$$

In the region near $P = P_i$, the first integrand is approximated by

$$\int_{P_i}^{P_{i-1}} f\left(P'\right) \mathrm{d}P' \approx \int_{P_i}^{P_{i-1}} \left(P'\right)^{n-1} \left(\frac{P' - P_i}{P'}\right)^{-1/2} \left(-\frac{\mathrm{d}X}{\mathrm{d}P}\right)_i \mathrm{d}P' \tag{3.72}$$

For $n = 0$

$$\int_{P_i}^{P_{i-1}} f\left(P'\right)\mathrm{d}P' \approx 2\ln\left(\frac{\sqrt{P_i + \Delta P} + \sqrt{\Delta P}}{\sqrt{P_i}}\right)\frac{\left(X_i - X_{i-1}\right)}{\Delta P}$$

For $n = 1$ (3.73)

$$\int_{P_i}^{P_{i-1}} f\left(P'\right)\mathrm{d}P' \approx \left[P_i \ln\left(\frac{\sqrt{P_i + \Delta P} + \sqrt{\Delta P}}{\sqrt{P_i}}\right) + \sqrt{\Delta P}\sqrt{\Delta P + P_i}\right]\frac{\left(X_i - X_{i-1}\right)}{\Delta P}$$

To compute the second integral, we can use the trapezoidal rule, which involves finite step discretization,

$$\int_{P_{i-1}}^{1-\Delta P} f\left(P'\right)\mathrm{d}P' \approx \Delta P\left(\frac{f_1 + f_{i-1}}{2} + \sum_{k=2}^{i-2} f_k\right) \tag{3.74}$$

where

$$f_k = \sqrt{\frac{\gamma - 1}{\gamma}}\left[P_k\right]^{n-1}\left[\frac{P_k}{P_i}\right]^{1/\gamma}\left[1 - \left(\frac{P_i}{P_k}\right)^{(\gamma-1)/\gamma}\right]^{-1/2}\left(-\frac{\mathrm{d}X}{\mathrm{d}P}\right)_k \tag{3.75}$$

In the third integral, X is small, and $P\left(X\right)$ may be expanded using a polynomial of the form

$$P\left(X\right) = 1 - \alpha X^2 + \ldots \tag{3.76}$$

Inserting Eq. (3.76) into the integral and assuming $\alpha\,\Xi^2 \ll 1$, we get

$$\int_{1-\Delta P}^{1} f\left(P'\right)\mathrm{d}P' \approx \sqrt{\frac{\gamma - 1}{\gamma}}\left(P_i\right)^{-1/\gamma}\left[1 - \left(P_i\right)^{(\gamma-1)/\gamma}\right]^{-1/2}\sqrt{\frac{\Delta P}{\alpha}} \tag{3.77}$$

To evaluate Eq. (3.77), α must be known beforehand. This is achieved by substituting Eq. (3.76) into Eq. (3.68) and extracting

$$\frac{1}{\sqrt{\alpha}}\int_0^X \frac{1}{\sqrt{X^2-\Xi^2}}\,\mathrm{d}\Xi = 1 \tag{3.78}$$

This enables us to deduce that $\alpha = \left(\frac{\pi}{2}\right)^2$.

Chapter 4

Results and Discussion

To characterize the effects of compressibility on the flow field in a rocket motor chamber, it is essential to verify our results. For this purpose, the solution is presented and compared to two closed-form analytical solutions developed under one-dimensional and two-dimensional, isentropic conditions.

4.1 Axisymmetric Configuration

In the treatment of the axisymmetric porous cylinder, Majdalani [29] uncovered a fully two-dimensional, closed-form analytical solution, validated with a numerical program. In his study, he closely examined the effects of compressibility and two dimensionality in a right-cylindrical chamber. With a uniform sidewall injection velocity driving the flow, his closed form mean flow solution was derived under isentropic conditions. In the interest of clarity, the solution obtained by Majdalani [29] is reproduced as:

$$\psi = M_w \psi_0 \left(1 - \tfrac{1}{4}\Gamma^2 \left[1 + \tfrac{1}{3}\cos(\pi r^2)\right]\chi^2 + \tfrac{1}{2}M_w^2\right) \text{ (stream function)} \qquad (4.1)$$

where $\psi_0 = x\sin(\tfrac{1}{2}\pi r^2)$ and $\chi = x / L_s$

$$M_c = \Gamma\chi \frac{2 + \tfrac{1}{3}\Gamma^2\chi^2 - M_w^2}{\sqrt{4 - 2(\gamma - 1)\Gamma^2\chi^2}}; \text{ (centerline Mach number)} \qquad (4.2)$$

$$p_c = 1 - \tfrac{1}{2}\gamma\Gamma^2\chi^2(1 - M_w^2) - \tfrac{1}{24}\gamma\Gamma^4\chi^4 \text{ (centerline pressure)} \qquad (4.3)$$

$$T_c = 1 - \tfrac{1}{2}(\gamma - 1)\Gamma^2\chi^2(1 - M_w^2) - \tfrac{1}{6}(\gamma - 1)\Gamma^4\chi^4 \text{ (centerline temperature)} \qquad (4.4)$$

where the sonic length, also known as the critical distance, is related to the Γ function through

$$\Gamma \equiv \pi M_w L_s = \sqrt{\lambda - 2\gamma - 2 + 2(2\gamma^2 + \gamma - 1)/\lambda} \qquad (4.5)$$

where

$$\lambda = \left(28 + 12\gamma - 6\gamma^2 - 8\gamma^3 + 6\sqrt{22 + 18\gamma - 6\gamma^2 - 14\gamma^3 - 3\gamma^4}\right)^{1/3} \qquad (4.6)$$

or, in expanded form,

$$\Gamma \cong 0.884622 - 0.177299(\gamma - 1) + 0.0539119(\gamma - 1)^2 - 0.0180615(\gamma - 1)^3 \qquad (4.7)$$

Another analytical solution found in the literature is a one-dimensional model used recently by Gany and Aharon [21]. Their relation is developed for an isentropic flow with the underlying assumption that the instantaneous burning rate [21] is uniform along the grain, thus leading to a constant mass flux at the simulated propellant surface. In summary, the one-dimensional model may be written as

$$M_{1D} = \sqrt{\frac{1-\sqrt{1-\chi^2}}{1+\gamma\sqrt{1-\chi^2}}} \tag{4.8}$$

$$P_{1D} = (1+\gamma)^{-1}\left(1+\gamma\sqrt{1-\chi^2}\right) \tag{4.9}$$

$$T_{1D} = (1+\gamma)^{1/\gamma-1}\left(1+\gamma\sqrt{1-\chi^2}\right)^{1-1/\gamma} \tag{4.10}$$

4.1.1 Critical Length

Concerning the calculation of the critical length, our computation of L_s leads to a sonic distance that matches the value predicted by Eq. (4.5), within 7%. On this note, it should be borne in mind that, according to Majdalani [29], the critical length denotes in the classic sense the distance from the headwall to the point at which the centerline velocity first reaches the speed of sound. At that station, the area-averaged Mach number would not have reached unity yet. However, in order to reconcile with one-dimensional predictions in which values are essentially area-averaged at a given axial station, a new definition is warranted, namely that of an area-averaged critical length, $\overline{L}_s$. Accordingly, a cross-section will be fully choked when the local average Mach number reaches unity. This condition always occurs at $\overline{L}_s > L_s$.

4.1.2 Pressure and Temperature

After solving Eq. (3.31) in decrements of ΔP, the pressure may be reproduced as a function of the axial distance. The resulting solutions for the centerline P and T are showcased in Figure 4.1 for $n = 0$ and $n = 1$. Also shown on the graphs are the

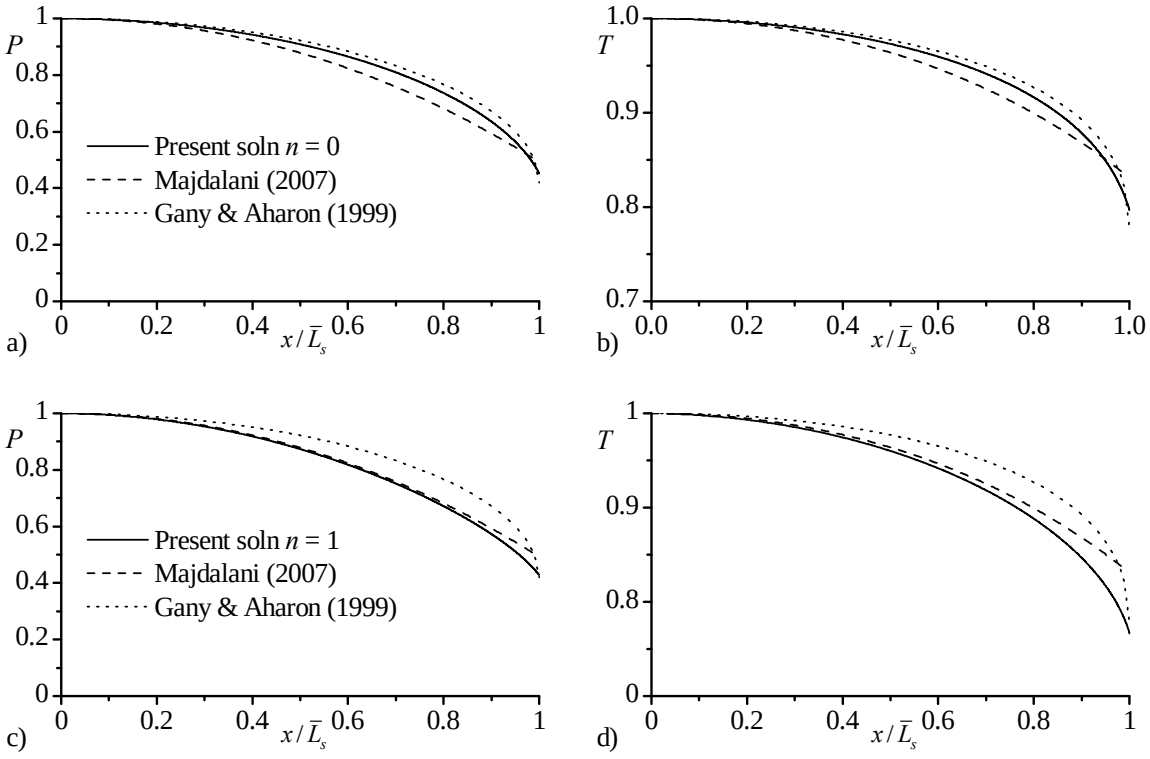

Figure 4.1. Comparison between the present semi-analytical formulation and both 1D and 2D solutions by Gany and Aharon [21] and Majdalani [29]. Results are shown for γ = 1.4 and M_w = 0.05.

analytical predictions based on the one-dimensional theory of Gany and Aharon [21] and the two-dimensional analysis of Majdalani [29].

Based on Figure 4.1, a qualitative agreement may be seen to be established between the present semi-analytical formulation, and Majdalani's closed form solution [29]. The same may be said of the one-dimensional solution of Gany and Aharon [21] despite its entirely dissimilar form. The small differences separating these estimates may be attributed to their underlying assumptions. The instantaneous burning rate of the one-dimensional solution [21] remains uniform along the grain, thus leading to a constant mass flux at the simulated propellant surface. A corresponding relation may be reproduced in the present solution by setting $n = 0,$ as reflected in the improved agreement with one-dimensional theory that may be inferred from Figures 4.1a-b. On the other hand, the uniform sidewall injection velocity of the two-dimensional axisymmetric solution of Majdalani [29] corresponds to the $n = 1$ case presented here. This may also explain the improved agreement with two-dimensional theory in Figures 4.1c-d.

In Figures 4.1a-b, the reason for the slight discrepancy at $n = 0$ may be attributed to the dismissal of radial pressure variations in the pseudo-two-dimensional formulation. As for the $n = 1$ case, the present model appears to be in excellent agreement with Majdalani's solution everywhere except in the vicinity of the choke point. Specifically, the tailing ends of the numerical curves in Figures 4.1c-d suddenly undergo an abrupt steepening process as the choke point is approached. This behavior causes a slight discrepancy to occur with respect to Majdalani's two-dimensional formulation [29]. Two possible explanations may be offered in this regard. The first attributes the attendant

divergence to the dismissal of radial pressure variations in the semi-analytical formulation, and to the linear approximation affecting pressure integration in Eq. (3.33). These approximations are likely to deteriorate near the choke point. The second source of disparity may be connected to the accuracy of Majdalani's Rayleigh-Janzen expansion in the vicinity of $x = \bar{L}_s$. However, according to Tollmien [32] and Kaplan [33], the Rayleigh-Janzen paradigm is formally shown to hold past sonic conditions. The first explanation is hence more plausible. On a separate subject, we remind the reader that the four parts of Figure 4.1 are obtained with an injection wall Mach number of 0.05. Nonetheless, these plots remain rather universal and therefore characteristic of the solution at other wall Mach numbers. This may be attributed to the results being displayed as function of the geometric similarity coordinate, $\bar{\chi} \equiv x / \bar{L}_s$.

4.1.3 Mach Number

A comparison of the centerline Mach numbers is provided in Figures 4.2a-b for $n = 0$ and $n = 1$, respectively. In both parts of this graph, the 2D analytical model is seen to outperform the 1D solution, although better agreement with the integral representation is realized in Figure 4.2b. This behavior may be naturally expected because the 2D model is derived under the $n = 1$ assumption. Another point of disparity may be associated with the centerline Mach numbers exceeding unity at $x = \bar{L}_s$. Conversely, the 1D Mach number, in which area-averaging is intrinsic, is seen to reach sonic conditions at $x = \bar{L}_s$. As shown in Figure 4.3, the analytical area-averaged Mach

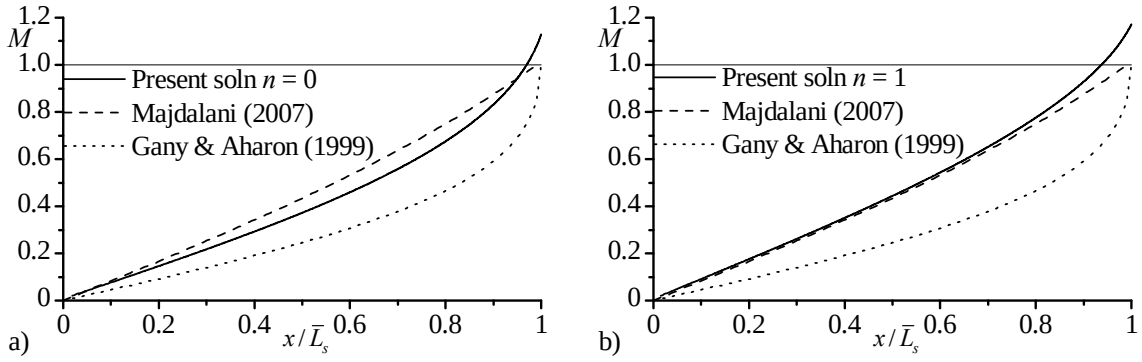

Figure 4.2. Evolution of centerline Mach numbers along with available 1D and 2D solutions. Here γ = 1.4 and M_w = 0.05.

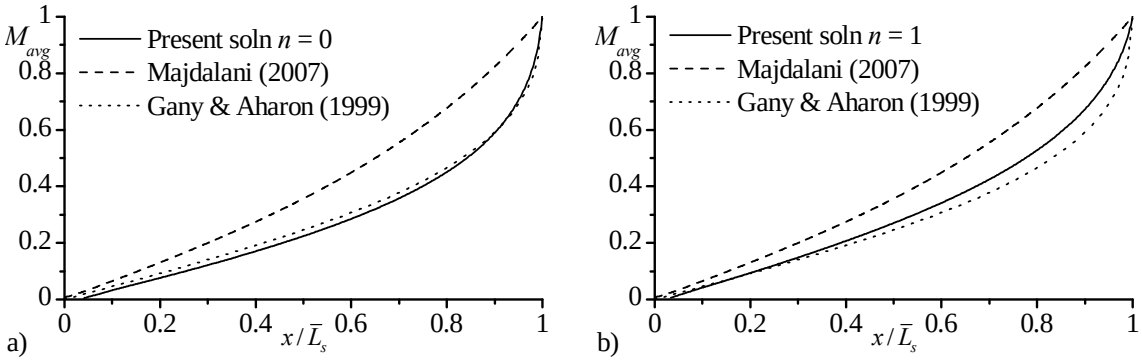

Figure 4.3. Comparison of the area-averaged Mach number of the present solution are the available 1D and 2D solutions.

number and the numerically area-averaged solution of the present formulation display steep curvatures that closely follow the dotted, 1D line.

It may be instructive to add that, based on Eq. (3.30), the Mach number may be calculated over the entire chamber. However, owing to the variables being expressed in terms of the axial location and the stream function leading tip ξ, a transformation is required to convert ξ back to the radial coordinate by way of Eq. (3.28). The results lead to a non-uniform mesh that requires careful treatment and "reverse engineering." After some effort, the contour plots of the numerically extracted local Mach numbers are displayed in Figure 4.4a, where the shape of the $M = 1$ curve is clearly delineated. The two-dimensional analytical predictions of the iso-Mach number lines are presented side-by-side in Figure 4.4b. Despite the dissimilarity in the contour curvature near choking (upper rightmost corner), the two models appear to display fairly good agreement in their predictions. Note that the traditional choking point is transformed, rather, into a curved

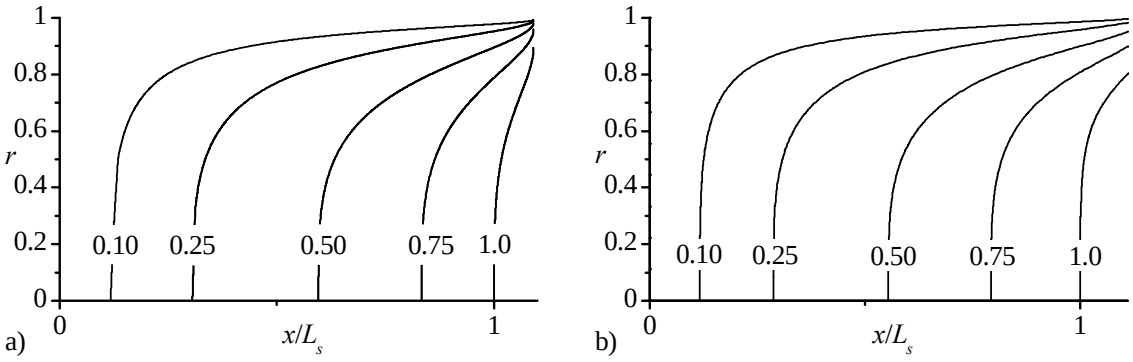

Figure 4.4. Local Mach number contours according to a) numerical integration and b) analytical solution by Majdalani [29]. Here γ = 1.4 and M_w = 0.01.

line and, in reality, to a surface due to axisymmetry; the latter can be captured either numerically, or analytically for $M = 1$. Note that Figures 4.2 and 4.3 are essentially universal and, being plotted versus x / L_s, will not change if a different wall Mach number is used at their basis. This again is due to the geometric self-similarity with respect to χ.

4.1.4 Streamlines

Having completed our description of the Mach number variation, characteristic streamlines are displayed in Figure 4.5 based on the numerical integration of Eq. (3.28). This is carried out by first specifying a value of ξ, and then integrating at discrete locations of x until the centerline Mach number has reached unity. This marks the critical distance to the sonic point and enables us to calculate L_s for each of the test cases at hand. The procedure also enables us to collect the family of coordinates at a fixed value of ξ, thus leading to an assortment of points that constitute a streamline. By comparing the results in Figure 4.5 at two wall Mach numbers of a) 0.01 and b) 0.005, it is clear that compressibility becomes more pronounced when the mean flow velocity is increased (here $\gamma = 1.4$). This is reflected in the faster flow turning that occurs at higher injection Mach numbers, specifically faster in Figure 4.5a where $L_s \cong 26.145$, than in Figure 4.5b where $L_s \cong 52.287$. However, by replotting these two cases versus x / L_s in Figures 4.5c-d, the ensuing graphs become identical! This is caused by the strong similarity with respect to χ.

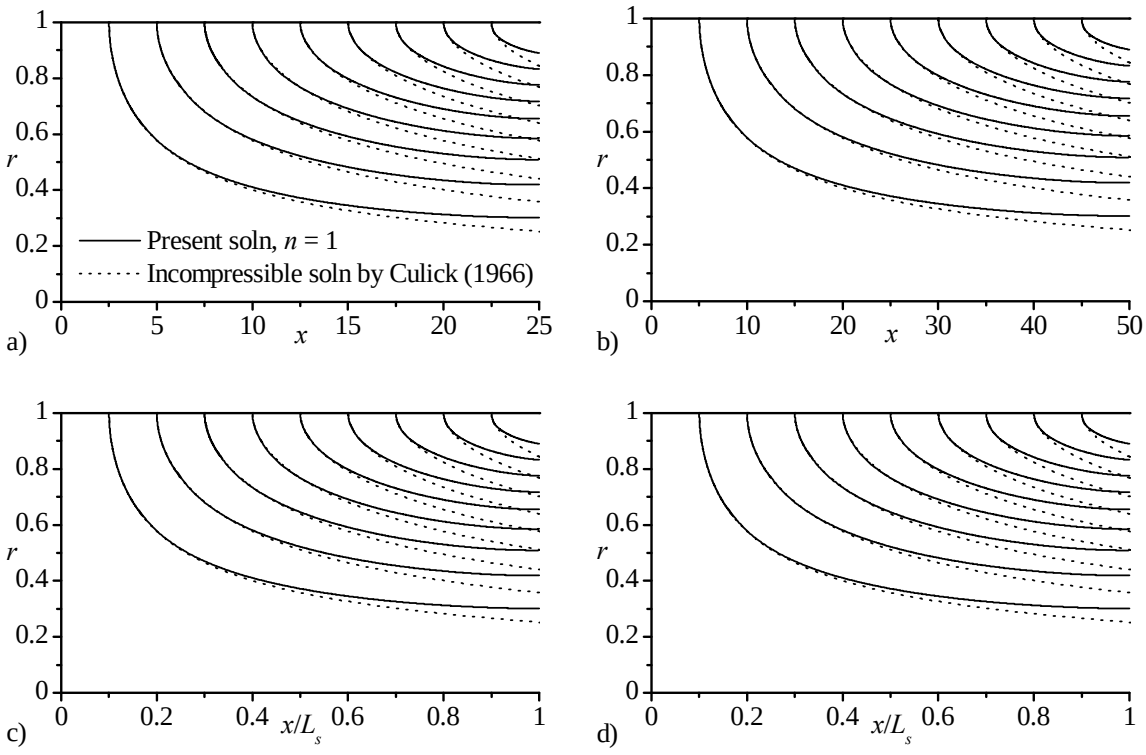

Figure 4.5. Numerical streamlines for a,c) M_w = 0.01 and b,d) M_w = 0.005 compared to the incompressible solution by Culick [3]. In c-d) the axial coordinate is rescaled by the critical length, thus leading to self-similarity.

4.1.5 Velocity Profiles

As one may infer from Figure 3.2, the last procedural step consists of extracting the axial velocity from Eq. (3.13). Forthwith, results are shown in Figure 4.6 at evenly spaced intervals of $x / L_s \approx 0.2, 0.4, \ldots, 1$. Also featured on the graph is Majdalani's 2D analytical solution [29]. By comparison to Taylor-Culick's incompressible mean flow solution [3], we note that the streamwise velocity develops into a much fuller, top-hat profile as choking is approached. The evolution into a blunter, turbulent-like, or pseudo-one-dimensional plug flow is conformant to both theory and experiment. It faithfully captures the increased gradients at the sidewall and these can have important implications in mean-flow related analyses.

Figure 4.7 presents the radial component of the velocity at multiple locations of

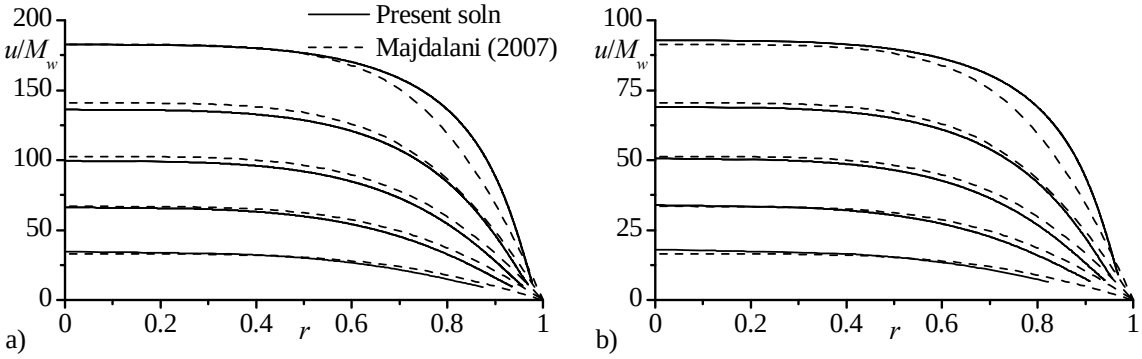

Figure 4.6. Spatial evolution of the axial velocity for a) M_w = 0.005 and b) M_w = 0.01 at x / L_s = 0.2, 0.4, 0.6, 0.8, and 1. Results are compared to the 2D axisymmetric solution by Majdalani [29]. Here γ = 1.4.

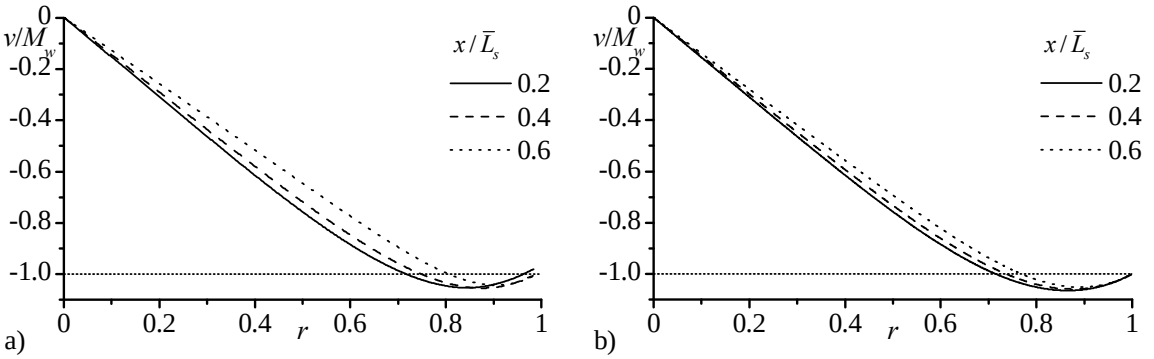

Figure 4.7. Spatial evolution of the radial velocity for M_w = 0.01 at x / L_s = 0.2, 0.4, 0.6 according to a) numerical integration and b) analytical solution by Majdalani [29].

the chamber, showing the evolution of the profile as the flow advances downstream. Alongside, Figure 4.7b demonstrates the results by Majdalani [29], exhibiting a good agreement between the two models.

4.2 Planar Configuration

When the same flow motion is considered in planar porous chambers, one may turn attention to Maicke and Majdalani [30] who were the first to construct a closed-form solution for the two-dimensional problem. Using techniques similar to the ones applied to the cylindrical case by Majdalani [29], they uncover compact expressions that describe the mean flow field in its entirety. For the reader's convenience, the Maicke-Majdalani model is summarized and reproduced as:

$$\psi = x\sin\left(\tfrac{1}{2}\pi y\right) + M_w{}^2\left[-\tfrac{1}{48}x\sin\left(\tfrac{1}{2}\pi y\right)\left\{\pi^2x^2\left[3+\cos\left(\pi y\right)\right]+3\left[7-\cos\left(\pi y\right)\right]\right\}\right] \quad (4.11)$$

$$P_c = 1 - M_{w^2}\gamma\left(\tfrac{1}{8}\pi^2 x^2\right) - M_{w^4}\left(\tfrac{1}{384}\gamma\pi^4 x^4 - \tfrac{3}{32}\gamma\pi^2 x^2 + \tfrac{1}{8}\gamma\right) \quad (4.12)$$

$$T_c = 1 + M_w^{\,2}\,\tfrac{1}{2}\left(1-\gamma\right)\left[\tfrac{1}{4}\pi^2 x^2\right] + M_w^4\left\{\tfrac{1}{192}\left(1-\gamma\right)\left[2\pi^4 x^4 - 18\pi^2 x^2 + 24\right]\right\} \quad (4.13)$$

$$L_s = \frac{1}{\pi M_w}\sqrt{\frac{\phi_a^{2/3} - 8\phi_a^{1/3}\left(\gamma+1\right) + 32\left(2\gamma^2+\gamma-1\right)}{\phi^{1/3}}} \quad (4.14)$$

where

$$\phi_a = -128\left[\left(4\gamma^3 + 3\gamma^2 - 6\gamma - 14\right)\right] + 3\sqrt{-\left(3\gamma^4 + 14\gamma^3 + 6\gamma^2 - 18\gamma - 22\right)} \quad (4.15)$$

Our integral formulation will also be compared to the curvature independent solution by Gany and Aharon [21], whose one-dimensional results have already been discussed in Section 4.1 in the context of axisymmetric motor.

4.2.1 Critical Length

The critical length calculated using the integral formulation matches the value predicted by Eq. (4.14) within 7%. It may be instructive to note that for a fixed wall Mach number, the sonic length for the planar motion is twice the value of its axisymmetric counterpart.

4.2.2 Pressure and Temperature

Equation (3.70) reports the principle integral expression linking the pressure to the axial distance. It is readily solved using the numerical approach described in Section 3.2.5. For constant mass flux ($n = 0$), results for the centerline pressure and temperature are illustrated in Figures Figure 4.8a and b respectively. The improved agreement

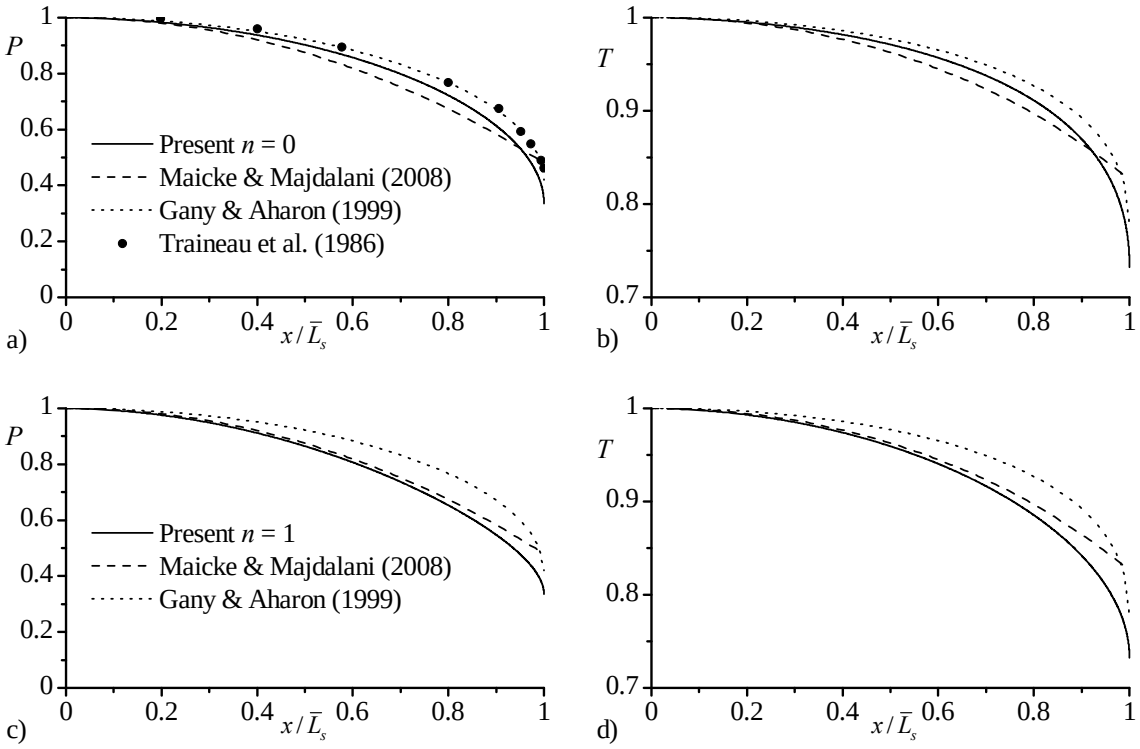

Figure 4.8. Comparison between the present semi-analytical formulation and both 1D and 2D solutions by Gany and Aharon [21] and Maicke and Majdalani [30], in addition to experimental results by Traineau et al. [15]. Results are shown for γ=1.4 and M_w = 0.05

between the one-dimensional expression and our model is justified by the virtue of their similar boundary conditions including the specification of uniform mass injection at the sidewall. Also shown on the figure are experimental data points acquired by Traineau et al. [15]. These researchers have also focused on the planar chamber with uniformly distributed mass addition. At first glance, it may be surprising to note the improved agreement that stands between experimental measurements and the one-dimensional model. This may be attributed to the dismissal of viscous effects which reduce the conversion of thermal energy to kinetic, thus building up the pressure in the chamber. Unlike the two dimensional model in which friction leads to additional increments in irreversibilities, the one dimensional model is less susceptible to these discrepancies due to its mass injection being fundamentally axial.

Figures 4.8c-d display the results for the $n = 1$ case. The present solution is in excellent agreement with the analytical relations by Maicke and Majdalani [30]. The slight disparity around the choking region may be connected to the linear approximations used in the numerical procedure. These approximations may deteriorate around the critical length.

4.2.3 Velocity Profiles

The evolution of the axial velocity profile throughout the chamber is illustrated in Figure 4.9 along with the 2D analytical solution by Maicke and Majdalani [30]. As expected, the results demonstrate similar behaviors as the flow travels downstream. Compared to the incompressible Taylor solution, the compressible profiles display a

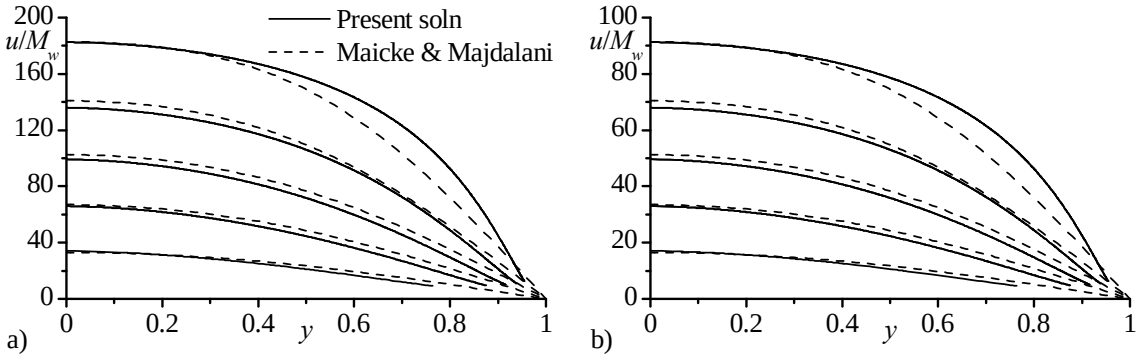

Figure 4.9. Spatial evolution of the axial velocity for a) M_w = 0.005 and b) M_w = 0.01 at x / L_s = 0.2, 0.4, 0.6, 0.8, and 1. Results are compared to the 2D axisymmetric solution by Maicke and Majdalani [30]. Here γ = 1.4.

steepening effect that is accompanied by higher velocity gradients near the wall. This steepening is also reflected in the experimental data collected by Traineau et al. [15].

Shown in Figure 4.10, a favorable agreement is seen to be established between the present solution and the experimental data, specifically at locations where the flow remains nearly incompressible, (i.e. before the flow reaches 40% of the chamber). Advancing further downstream, steepening occurs and appears to be more pronounced in the experimental data. The disparity is justified by the dismissal of viscous and turbulence effects which may become more pronounced as the flow approaches the critical length.

4.2.4 Streamlines

By specifying a value of ξ and integrating along x, one can extract the streamlines. These are displayed in Figure 4.11 side by side with the incompressible

streamlines from Taylor [2]. Note that the effects of compressibility translate into faster turning of the flow. In Figure 4.11b, the axial distance is rescaled by the sonic length.

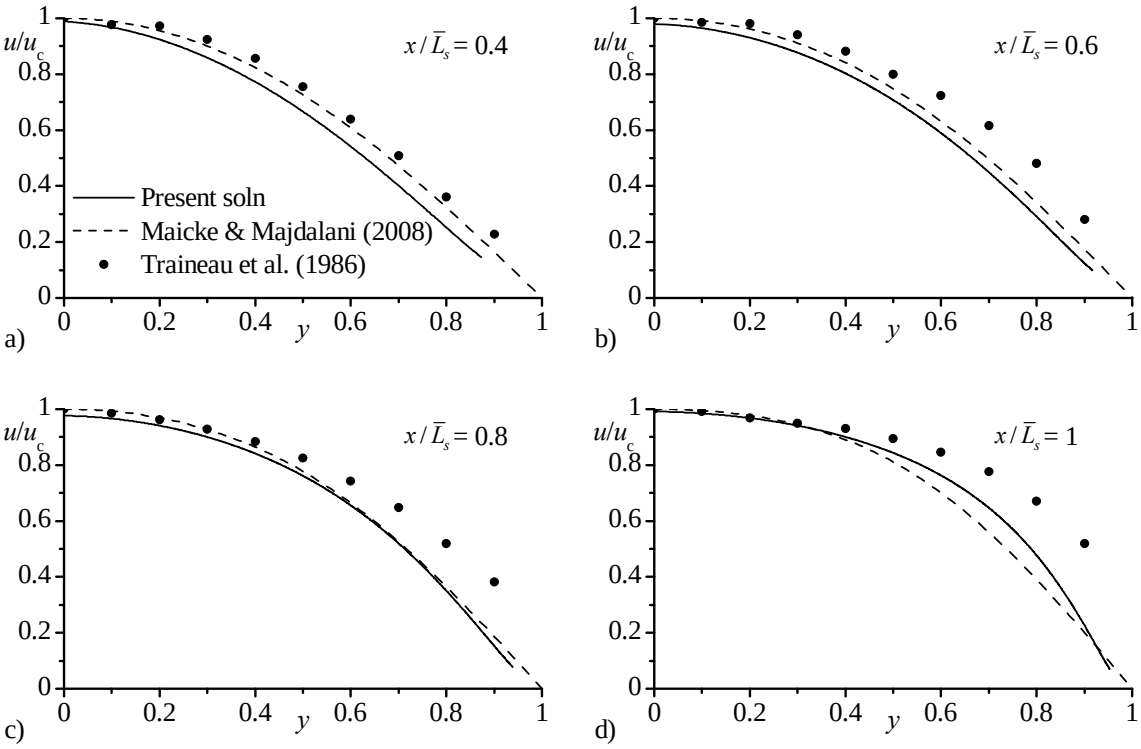

Figure 4.10. Axial velocity profiles obtained using the present formulation, the analytical solution by Maicke and Majdalani [30], and experimental data taken from Traineau et al. [15].

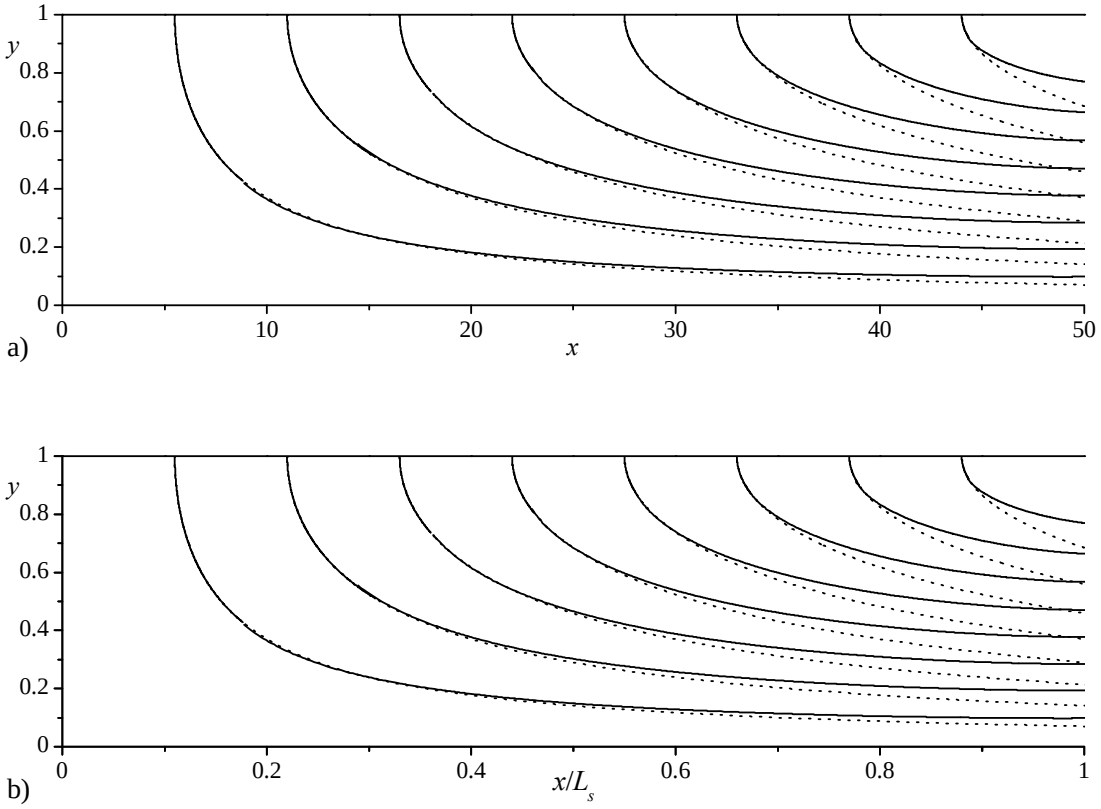

Figure 4.11. Numerical streamlines for M_w = 0.01, depicted in solid lines, compared to the incompressible solution by Taylor [2], represented in dotted lines. In b) the axial coordinate is rescaled by the critical length, thus leading to self-similarity.

Chapter 5

Conclusions

In this study, the integral formulation of the porous chamber initiated originally by Traineau, Hervat and Kuentzmann [15], and later extended by Balakrishnan, Liñan and Williams [28], is reconstructed and compared to one- and two-dimensional analytical approximations obtained under isentropic flow conditions. Unsurprisingly, the level of agreement with the integral representation is found to be commensurate with the sidewall boundary conditions associated with each of these models. Being derived for a uniform mass flux at the sidewall, the one-dimensional model seems to provide closer predictions to the inverted integral solution with a pressure exponent of $n = 0$. Such a condition suppresses the velocity dependence on the pressure and ensures a constant mass flux at the sidewall. Conversely, the $n = 1$ case leads to a constant wall-normal velocity that coincides with one of the boundary conditions used in deriving the two-dimensional analytical models [29]. Consequently, numerical predictions for this case fall in closer agreement with the two-dimensional solution. In all cases, the main discrepancies occur

near the sonic point and may be attributed to the various forms of approximations and linearizations befalling the integral approach. Furthermore, when comparing the level of difficulty needed to reproduce these solutions, the closed-form analytical approximations seem to substantially outperform the semi-analytical treatment. The latter requires piecewise numerical integrations, sequential inversions, and backward transformations to retrieve the original variables of interest. As if these multiple operations are not enough, the problem is further exacerbated by the variable extraction process occurring over a highly non-uniform mesh. This can render simple steps extraordinarily challenging, especially when attempting to extrapolate other related variables and derivatives that are needed over a uniform grid. Such effort can be quite laborious when compared to the ease with which the fully analytical models are implemented and resolved. Nonetheless, the numerical formulation helps to confirm several useful characteristics associated with the two-dimensional theory introduced previously by Majdalani [29], and Maicke and Majdalani [30]. Among them is the strong, albeit non-exact, self-similarity with respect to the critical length. This can be seen by rescaling the axial coordinate with respect to $\bar{L}_s$; numerically obtained streamline, pressure, and temperature plots taken at two different Mach numbers become visually identical. The observed behavior confirms two-dimensional theory which, in turn, projects deviations from self-similarity to be of the order of the wall Mach number squared, a practically small quantity that leads to relative differences of less than 1%.

While this study captures the compressibility effects on the mean flow field in rocket motors, the model can be improved for a better prediction of the parameters involved.

The comparison of our model with experimental data showed some discrepancy as the flow gets closer to the sonic length. For future considerations, it is imperative to study the influence of viscous and turbulence effects on the flow.

References

References

[1] Berman, A. S., 1953, “Laminar Flow in Channels with Porous Walls,” J. Appl. Phys., 24, No. 9, pp. 1232-1235.

[2] Taylor, G. I., 1956, “Fluid Flow in Regions Bounded by Porous Surfaces,” Proc. R. Soc. Lond., **234**, No. 1199, pp. 456-475.

[3] Culick, F. E. C., 1966, “Rotational Axisymmetric Mean Flow and Damping of Acoustic Waves in a Solid Propellant Rocket,” AIAA J., **4**, No. 8, pp. 1462-1464.

[4] Dunlap, R., Blackner, A. M., Waugh, R. C., Brown, R. S., and Willoughby, P. G., 1990, “Internal Flow Field Studies in a Simulated Cylindrical Port Rocket Chamber,” J. Propul. Power, **6**, No. 6, pp. 690-704.

[5] Saad, T., and Majdalani, J., 2009, “Rotational Flowfields in Porous Channels with Arbitrary Headwall Injection,” J. Propul. Power, **25**, No. 4, pp. 921-929.

[6] Majdalani, J., and Saad, T., 2007, “The Taylor-Culick Profile with Arbitrary Headwall Injection,” Phys. Fluids, **19**, No. 9, pp. 093601-10.

[7] Zhou, C., and Majdalani, J., 2002, “Improved Mean Flow Solution for Slab Rocket Motors with Regressing Walls,” J. Propul. Power, **18**, No. 3, pp. 703-711.

[8] Majdalani, J., Vyas, A. B., and Flandro, G. A., 2002, “Higher Mean-Flow Approximation for a Solid Rocket Motor with Radially Regressing Walls,” AIAA J., **40**, No. 9, pp. 1780-1788.

[9] Sams, O. C., Majdalani, J., and Saad, T., 2007, “Mean Flow Approximations for Solid Rocket Motors with Tapered Walls,” J. Propul. Power, **23**, No. 2, pp. 445-456.

[10] Saad, T., Sams, O. C., and Majdalani, J., 2006, “Rotational Flow in Tapered Slab Rocket Motors,” Phys. Fluids, **18**, No. 1, pp. 103601-13.

[11] Kurdyumov, V. N., 2006, “Steady Flows in the Slender, Noncircular, Combustion Chambers of Solid Propellants Rockets,” AIAA J., **44**, No. 12, pp. 2979-2986.

[12] Majdalani, J., and Saad, T., 2007, “Energy Steepened States of the Taylor-Culick Profile,” *AIAA* 2007-5797, Cincinnati, OH.

[13] Saad, T., and Majdalani, J., 2008, “Energy Based Mean Flow Solutions for Slab Hybrid Rocket Chambers,” *AIAA* 2008-5021, Hartford, CT.

[14] Dunlap, R., Willoughby, P. G., and Hermsen, R. W., 1974, “Flowfield in the Combustion Chamber of a Solid Propellant Rocket Motor,” AIAA J., **12**, No. 10, pp. 1440-1445.

[15] Traineau, J. C., Hervat, P., and Kuentzmann, P., 1986, "Cold-Flow Simulation of a Two-Dimensional Nozzleless Solid-Rocket Motor," *AIAA* 86-1447.

[16] Beddini, R. A., 1986, "Injection-Induced Flows in Porous-Walled Ducts," AIAA J., **24**, No. 11, pp. 1766-1773.

[17] Baum, J. D., Levine, J. N., and Lovine, R. L., 1988, "Pulsed Instabilities in Rocket Motors: A Comparison between Predictions and Experiments," J. Propul. Power, **4**, No. 4, pp. 308-316.

[18] Liou, T.-M., and Lien, W.-Y., 1995, "Numerical Simulations of Injection-Driven Flows in a Two-Dimensional Nozzleless Solid-Rocket Motor," J. Propul. Power, **11**, No. 4, pp. 600-606.

[19] Apte, S., and Yang, V., *Effect of Acoustic Oscillation on Flow Development in a Simulated Nozzleless Rocket Motor, Solid Propellant Chemistry, Combustion, and Motor Interior Ballistics*, Yang, V., T. B. Brill, and W.-Z. Ren eds., AIAA Progress in Astronautics and Aeronautics, Washington, DC, 2000, Vol. 185, 791-822.

[20] Apte, S., and Yang, V., 2001, "Unsteady Flow Evolution in a Porous Chamber with Surface Mass Injection. Part I: Free Oscillation," AIAA J., **39**, No. 8, pp. 1577-1586.

[21] Gany, A., and Aharon, I., 1999, "Internal Ballistics Considerations of Nozzleless Rocket Motors," J. Propul. Power, **15**, No. 6, pp. 866-873.

[22] King, M. K., 1987, “Consideration of Two-Dimensional Flow Effects on Nozzleless Rocket Performance,” J. Propul. Power, **3**, No. 3, pp. 194-195.

[23] Venugopal, P., Najjar, F. M., and Moser, R. D., 2001, “Numerical Simulations of Model Solid Rocket Motor Flows,” *AIAA* 2001-3950, Salt Lake City, Utah.

[24] Wasistho, B., Balachandar, S., and Moser, R. D., 2004, “Compressible Wall-Injection Flows in Laminar, Transitional, and Turbulent Regimes: Numerical Prediction,” J. Spacecraft Rockets, **41**, No. 6, pp. 915-924.

[25] Najjar, F. M., Haselbacher, A., Ferry, J. P., Wasistho, B., Balachandar, S., and Moser, R., 2003, “Large-Scale Multiphase Large-Eddy Simulation of Flows in Solid-Rocket Motors,” *AIAA* 2003-3700, Orlando, FL.

[26] Wasistho, B., Haselbacher, A., Najjar, F. M., Tafti, D., Balachandar, S., and Moser, R. D., 2002, “Direct and Large Eddy Simulations of Compressible Wall-Injection Flows in Laminar, Transitional, and Turbulent Regimes,” *AIAA* 2002-4344.

[27] Shapiro, A. H., *The Dynamics and Thermodynamics of Compressible Fluid Flow*, The Ronald Press Company, 1953, Chap. 1.

[28] Balakrishnan, G., Liñan, A., and Williams, F. A., 1991, “Compressible Effects in Thin Channels with Injection,” AIAA J., **29**, No. 12, pp. 2149-2154.

[29] Majdalani, J., 2007, “On Steady Rotational High Speed Flows: The Compressible Taylor-Culick Profile,” Proc. R. Soc. Lond., **463**, No. 2077, pp. 131-162.

[30] Maicke, B. A., and Majdalani, J., 2008, “On the Rotational Compressible Taylor Flow in Injection-Driven Porous Chambers,” J. Fluid Mech., **603**, No. 1, pp. 391-411.

[31] Balakrishnan, G., Liñan, A., and Williams, F. A., 1992, “Rotational Inviscid Flow in Laterally Burning Solid Propellant Rocket Motors,” J. Propul. Power, **8**, No. 6, pp. 1167-1176.

[32] Tollmien, W., 1941, “Grenzlinien Adiabatischer Potentialströmungen.,” J. Appl. Math. Mech. (ZAMM), **21**, No. 3, pp. 140-152.

[33] Kaplan, C., 1946, “Effect of Compressibility at High Subsonic Velocities on the Lifting Force Acting on an Elliptic Cylinder,” *Langley Memorial Aeronautical Laboratory, National Advisory Committee for Aeronautics NACA* No. 834, pp. 49-57.

Vita

Michel Akiki was born in Jounieh, Lebanon on October 29, 1984. In the spring of 2007, he received his Bachelor's of Engineering in Mechanical Engineering from Notre Dame University. During his undergraduate studies, Michel continued taking piano lessons to build up his 12 years of practice in classical music. Michel studied Fluid Mechanics under the direction of Dr. Majdalani at the University of Tennessee Space Institute and will be graduating with a Master of Science degree in Aerospace Engineering in December of 2009. Michel plans to continue his studies at the University of Tennessee Space Institute to pursue his doctoral degree.